Research Square

Preprints are preliminary reports that have not undergone peer review.
They should not be considered conclusive, used to inform clinical practice,
or referenced by the media as validated information.

Phytoconstituent Effect on Morphology of ZnO nanostructure: Synthesis, characterisation and photocatalytic degradation of Methylene blue, Malachite green, Brilliant cresyl blue, Rb171, Eosin yellow and Congo red dye

SUNEEL -

suneelphd@student.iul.ac.in

Research lab-B043, Department of Chemistry, Integral University, Lucknow , Uttar Pradesh 226026

Haroon -

Department of Physics, Integral University, Lucknow, Uttar Pradesh 226026

Mohd. Shabbir

Department of computer application, Integral University, Lucknow, Uttar Pradesh 226026

Zainab Feroz

Integral Centre of Excellence for Interdisciplinary Research, IUL

Nafees Ahmad

Research lab-B043, Department of Chemistry, Integral University, Lucknow , Uttar Pradesh 226026

Qazi Inamur Rahman

Research lab-B043, Department of Chemistry, Integral University, Lucknow , Uttar Pradesh 226026

Research Article

Keywords: Sol-gel, phytogenic route, tannins, zetapotential, Hydrodynamic diameter, Hazardous

Posted Date: June 23rd, 2026

DOI: https://doi.org/10.21203/rs.3.rs-9250725/v1

License: This work is licensed under a Creative Commons Attribution 4.0 International License.
Read Full License

Additional Declarations: No competing interests reported.

"Phytoconstituent Effect on Morphology of ZnO nanostructure: Synthesis, characterisation and photocatalytic degradation of Methylene blue, Malachite green, Brilliant cresyl blue, Rb171, Eosin yellow and Congo red dye"

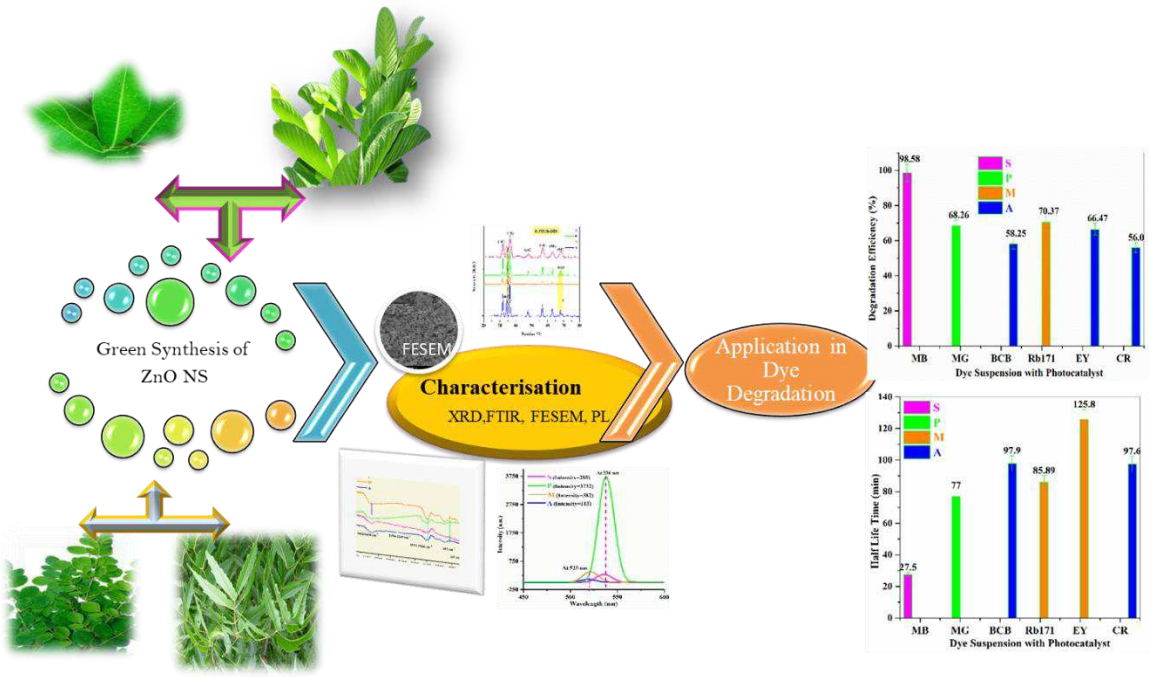
Suneel [a*], Haroon [b] , Mohd. Shabbir[c], Zainab Feroz[d], Nafees Ahmad [a,] Qazi Inamur Rahman [a*],
[a] *Research lab-B043, Department of Chemistry, Integral University, Lucknow (IUL), Uttar Pradesh 226026, India*
[b]*Department of Physics, Integral University, Lucknow, Uttar Pradesh 226026, India.*
[c] *Department of computer application, Integral University, Lucknow, Uttar Pradesh 226026, India.*
[d]*Integral Centre of Excellence for Interdisciplinary Research, IUL,226026 U.P., India*
Corresponding author: Suneel (M.Sc. M.Tech.) suneelphd@student.iul.ac.in
Dr.Qazi inamur Rahman : qirahman@iul.ac.in

Abstract

The aim of this research is to study the effect of different phytochemicals on the photocatalytic performance and yield of nonhazardous ZnO NS, synthesised by a sustainable sol-gel phytogenic route. $(CH_3COO)_2Zn.2H_2O$ was used as a source of Zn^{2+}, while polyphenols, tannins present aqueous leaf extracts (pressurized liquid extraction method) of *Syzygium cumini*, *Psidium guajava, Moringa oleifera* and *Azadirachta indica* work as bio-reductants and capping agents. The percentage yield of ZnO NS of *P. guajava* is the highest, followed by *S. cumini*. The XRD (X-ray Diffraction) analysis revealed a high-purity hexagonal wurtzite phase, size ranging from 6.68-13.76 nm. FTIR spectra identified a characteristic ZnO vibrational band ~618 cm^{-1} in all green-derived samples. DRS, surface charge and size characterisation confirm the band gap energy of 2.90, 2.66, 2.74 and 2.92 eV, zetapotential -23.7, -28.1, 24.3 and -28.6 mV, and average hydrodynamic diameter are 463, 603.9, 574.5 and 276.7 nm for samples S, P M and A, respectively. In this sequence for morphological analysis, histogram particle size distribution, elemental overlay, and e^-/h^+ (electron-hole) recombination rate was characterised by FESEM coupled with EDX and PL spectroscopy. This difference in size, ζ, and morphology indicates that the specific phytochemical profile of the leaf extract significantly modulates the optical properties, particle size and surface charge. Moreover, the sunlight photocatalytic efficiency of biosynthesized ZnO NPs was demonstrated over cationic (MB, MG, BCB) and anionic (RB171 EY and CR) dyes as model pollutants. Nearly 93.58, 66.83, and 57.27% degradation of MB, MG, and BCB were achieved within 120 min, whereas Rb171, Ey, and CR exhibited a comparatively lower removal efficiency of approximately 46.74, 43.72, and 50.52% over the same duration with sample S. The degradation of kinetics was consistent with the pseudo–first-order model, k_{app} of 0.02524, 0.00882, 0.0065, 0.00474, 0.00472 and 0.0056 min^{-1} for MB, MG, BCB, Rb171, EY and CR, respectively, with a half-life period of ~27.50, 78.75, 106.48, 146.20,146.80 and 138.8 min. Comparative examination of mineralization and calculated kinetic parameters revealed a preferential photocatalytic affinity of photocatalyst toward cationic dyes. These findings conclude that plant-derived NPs offer a good performance and environmentally friendly photocatalyst in the degrading of hazardous dye effluent present in aqueous systems in solar light.

Keyword: Sol-gel, phytogenic route, tannins, zetapotential, Hydrodynamic diameter, Hazardous

Graphical Abstract



1. Introduction

The rapid growth of human population, unrelenting urbanization in the world and the leaning, towards modernization has increased the demand of industrial revolution, which tend to move towards plantation of industries like paper, tanning and textile. Among these, textile industry is a very important feature of this landscape that satisfies some of the key anthropogenic demands. Dyeing, printing, and finishing processes are involved in textile operations that require the use of a lot of organic and synthetic pigments. There are over 10000 dyes in which 60-80 % are azo dyes. Annually 60% produced dyes are consumed in textile industries [1-2]. Approximately 10–15% of dyes do not fix to fabrics and are discharged directly into effluents. Annually, an estimated 280,000 tons of textile dyes are released into global water systems [3-4]. Textile industries utilised huge number of water (1kg fabric=75-150kg water) and wide range of various pollutants that include organic and inorganic dyes effluents, heavy metal (e.g. Co, Cr, Ni, Cu, Pb and Hg), and antioxidants and variety of hazardous non-biodegradable substance which are discharge in to water and surrounding atmosphere [5]. These pollutants significantly lower the levels of dissolved oxygen (DO) in aqueous environments. The subsequent declined in dissolved oxygen increases the biological oxygen demand (BOD) of water masses, shows negative impact on the marine life and human health. Such levels of pollution exceed ecological boundaries hence posing a serious challenge to the environment. Most common synthetic azo dyes (-N=N=) like congored (CR), Methyl orange (MO), Acid orange 20(AO20) (MO) (60-70%), and non-azo dyes

(MB, RhB, BCB, MG and EY), can break down into carcinogenic aromatic amines which linked to sever long term hazards like skin cancer, toxicity, genotoxicity and mutagenicity [6-8]. Thus, removal of dyes effluents from aqueous matrices is one of the major environmental concerns in water purification and reducing the pollution level. In the past, decade several physical techniques (solvent extraction, membrane filtration ion exchange, coagulation-flocculation, RO, electrodialysis, adsorption, sorption), chemical method like ozonation, electrochemical oxidation, chemical precipitation, physiochemical and bioremediations process (aerobic and anaerobic, microbial)that have been used[9-10].These physical, chemical and biological techniques are time consuming, required continuous replacement of membrane, high cost and high energy demands and utilization of chemical reagent, and high experimental condition and produces secondary waste streams, sediments particles, that require additional cleanup [11-12].Fig.1. shows the source of dye effluents and efficiency of various methods and their efficiency to remove dye effluents.

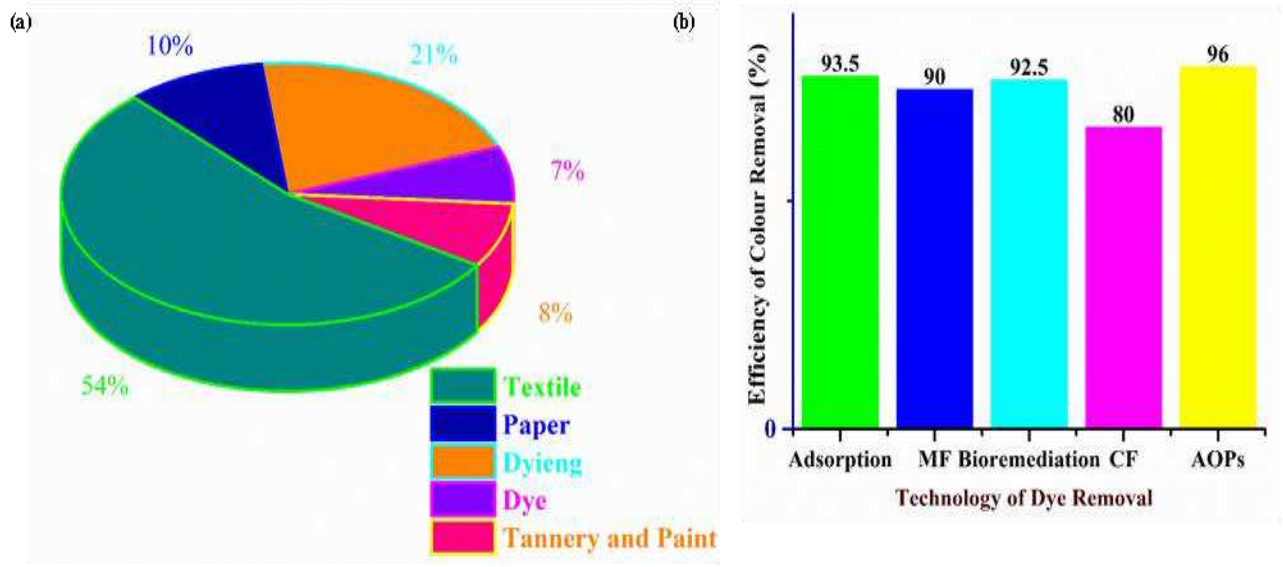


Fig.1 (a) Source of dyes effluents and, (b) Efficacy of physical, biological method to remove dye from water bodies.

In this regard there is a lot of scholarly interest regarding use of photocatalytic nanomaterials, which work on advanced oxidation processes (AOPs), since it has been found to be more effective for degradation, decolorization and mineralization of dye pollutants in presence of solar light through photocatalytic oxidation [13]. Apart from using modern technology metal and nonmetal doped, nanomaterials key to achieving because of large surface area, easy synthesis, the choice of catalysts as depending on pollutants, reusability and total elimination of organic contaminates without generation secondary pollutants that required additional processing [14].Several metal and metal oxide based photocatalyst including SnO_2, ZrO_2, TiO_2, MnO_2, ZnS, WO_3 [15], Cu_2S [16], FeO [17], α-Fe_2O_3 [18], CeO_2[19], TiO_2 (Eg=3.2eV, only 5% conversion of sunlight) and ZnO [20] have proven to be effective photocatalysts in degradation of dyes in to environmentally benign

products. ZnO stands out as II-VI semiconductor and an excellent visible photocatalyst due to its moderate optical band gap energy (Eg=~3.7eV), elevated photosensitivity in natural sunlight, insignificant cost of its metal precursors, non-toxicity, aqueous stability and enhanced isoelectric point [21]. A series of ZnO NPs were prepared through solvothermal [21], sol-gel [22-23], precipitation [24-25], hydrothermal [26], co-precipitation [27], solution-based method [28] that showed good photocatalytic activity in presence of light. M.F. Abdel Messih et al synthesised novel Ag/ZnO, by sol-gel method using chitson as reducing, that degraded 81.2 % MB dyes in 240 min of UV irradiation [29]. Despite the established precision of chemical synthesis of ZnO NPs that has uncontrolled morphology, particle size, wastage of chemical, environmental risks, high energy demands have shifted the research toward biogenic [30], green routes for synthesis of ZnO NPs. This method offers a sustainable alternative by utilizing plant-derived phytochemicals [31], such as flavonoids and polyphenols as natural reducing and capping agents, often resulting in ZnO NPs with reduced Eg, and excitation B.E.(60meV), excellent photocatalytic activity, and enhanced antimicrobial [32], antibacterial, antioxidant anticancerous activity [33], ecofriendly compared to those produced via traditional chemical methods. In recent years, special attention efforts have been focused at the plant-mediated synthesis of ZnO NPs as a sustainable alternative to conventional chemical routes. Prime examples include the use of flower of *Hibiscus sabdariffa* [34], fruit *Garcinia Cambogia [35]*, *Myristica fragrans* [36], *Rubus coreanus* [37], *Garcinia mangostana* [38], jujube extract [39], *Amomum nonglobular [40]* studied the potential of phytochemical precursors to fabricate morphological, and catalytic properties of eco-friendly synthesised ZnO NPs Later on Fatemeh et al., [41] syntheised the ZnO NPs using Lemon juice and studied its photocatalytic efficiency over MO (10ppm), MB(5ppm), MR(25ppm) under UV radiation. Kuruppu et al. [42] Phyto fabricated ZnO NPs utilising peel and seed of *N. lappaceum L.* and *G. mangostana L.* that degraded 97% MB dyes in 150 min of solar light irradiation. Vinayagam et al. [43] and Babitha *et al.* [44] synthesised nanoflower and nanosheet ZnO using leaf extract and studied its degradation performance over MB dyes. Studies of the nature of phytochemical extract present in leaves on the optical and photocatalytic efficiency of ZnO NPs were carried out by J. Osuntokun et al. [45], Gawade *et al.* [46], Aldeen et al. [47], Sreelekshmi et al. [48], Vasantharaj *et al.* [49], O et al. [50], Rajendra *et al.* [51], Karthik *et al.* [52], Razia et al. [53] and Abomuti *et al*.[54]. In previous years, Phyto-fabrication of ZnO NPs and Ns such as *Syzygium cumini* (*S. cumini*) [55], *Psidium guajava (P. guajava)* [56-57], *Moringa oleifera (M. oleifera)*[58-60], and *Azadirachta indica (A. indica)* [61-63] has been reported, and their photocatalytic efficiency has been demonstrated over different dyes.

The objective of this research to investigates the synthesis yield of ZnO NPs through a phytogenic route utilizing *S.cumuni, P.guajava, M.oleifera* and A.*indica* leaves extract and $(CH_3CO_2)_2Zn.2H_2O$ precursor followed by evaluation of their ability to induce photo-oxidative decomposition and progressive mineralization of cationic (MB, MG, BCB,) and anionic (Rb171, EY CR) dyes in solar light irradiation, leading to the formation of nontoxic products. The approach aims a sustainable synthesis pathway coupled with an environmentally benign strategy for wastewater remediation of dyes effluents coming from textile and other industry.

2. Material Experimental procedure

2.1. Chemical and Plant leaf

Zinc acetate dihydrate (ZAD), Zn $(CH_3COO)_2.2H_2O$ (99%), ethyl alcohol (C_2H_5OH,95%), were purchased from Gyan scientific, Lucknow U.P. India, and used without any purification. Milli Q water was used during all the experimental work available in CIF (central Instrumentation Facility) IUL campus. Fresh leaves of the *S. cumini, P. guajava M. oleifera* and *A. indica,* were collected afternoon in month of February,2025 from the Aliganj, Sahara state and Jankipuram, area of Lucknow U.P. India.

Table.1 Physical properties of dyes used in this study [1,7,10,35,37]

Characteristics Properties	Methylene Blue MB	Brilliant cresyl blue (BCB)	Malachite green (MG)	Reactive blue Rb171	Congo Red (CR)	Eosin Yellow (EY)
Chemical Formula	$C_{16}H_{18}ClN_3S$	$C_{17}H_{20}ClN_3O$	$C_{23}H_{25}ClN_2$	$C_{40}H_{22}Cl_2N_{15}Na_3O_{19}S_6$	$C_{32}H_{22}N_6Na_2O_6S_2$	$C_{20}H_6Br_4Na_2O_5$
M.W. (g/mol)	319.85	318	364.91	1433.95	696.7	647.89
Class of dyes	Basic	Basic	Basic	Acidic	Acidic	Acidic
λmax (nm)	664-665	625-630	614-616	610-625	497-500	515-518
Transition	n →π*	n→π*	π→π*	π→π*	π→π*	π→π*
Major use	Pharmaceutical and Textile	Hematology	Leather, Silk, Antifungal	Cotton, Textile dyeing	Amyloid detection	Cytoplasmic stain

2.2 Preparation of leaves extract

The fresh leaves *S.cumini, P.guajava*, *M.oleifera* and *A. indica* were first washed with tap water, followed by distilled water to remove dust particles, and kept under shade sunlight for 10day; until the leaves became completely dry. The dried leaves were cut into small pieces and then pulverized using a blender. In order to prepare the leaf extract, 20 g of leaves powder of each plant were separately mixed with 200 ml of $_{d.}H_2O$ and placed on a magnetic stirrer at 60^0C for approximately 30 minutes, until a pale brown solution was achieved. The resulting solution was left to cool at 25°C±. The pH of the resulting solution was quite close to neutral (~7), which was excellent. Afterwards, the prepared solution of leaf extract was filtered using Whatman no.42 filter paper and filtrate was collected in a reagent bottle and stored at 4 ◦C in the refrigerator for green synthesis of ZnO NPS of *S. cumini (***S***), P. guajava*, (**P**), *M. oleifera* **(M)**, *A. indica* (**A**).

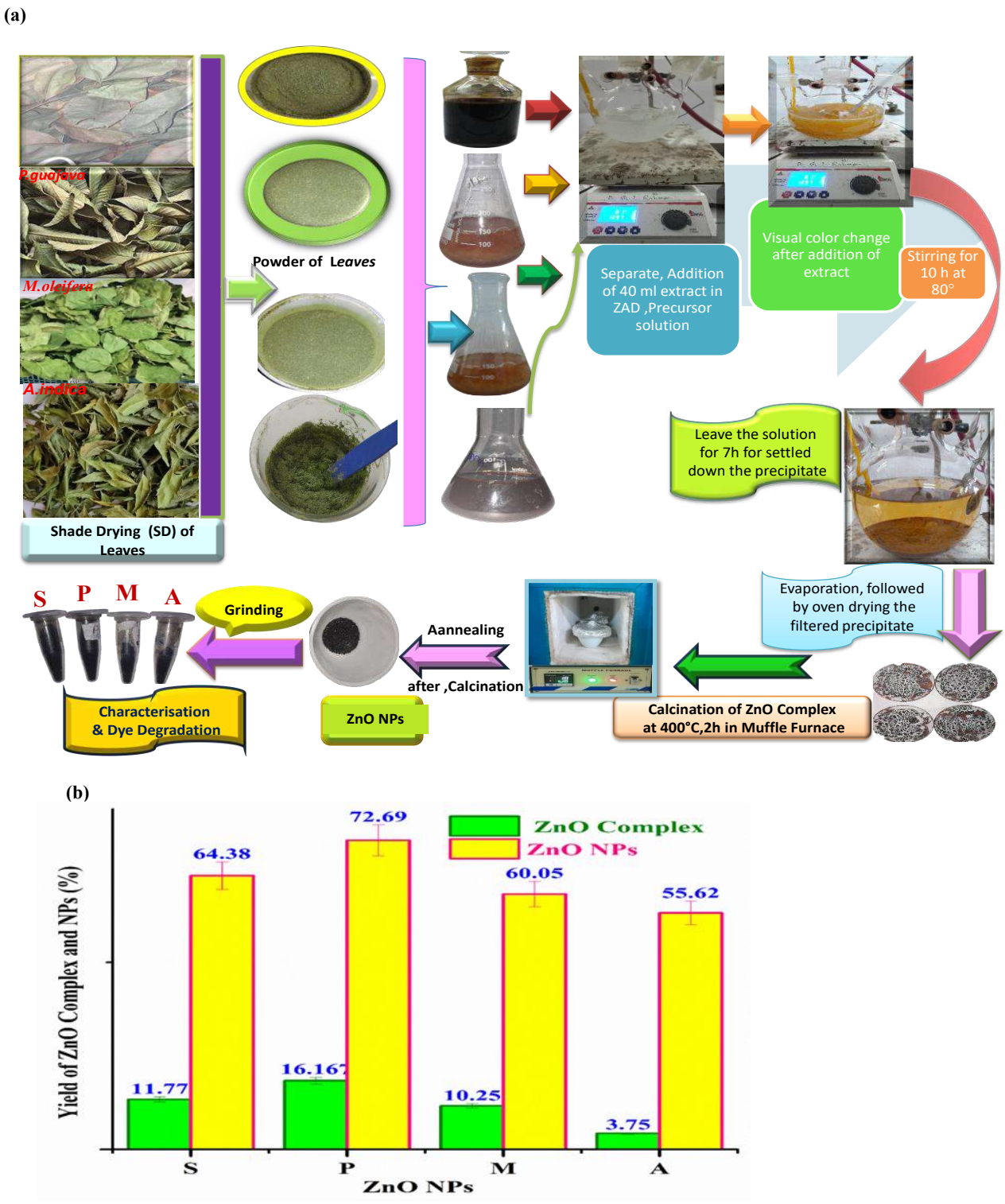


Fig.2 (a)Schematic route for synthesis of ZnO NS sample (S,P,M and A) and (b) Average yield ZnO dried complex (yellow)) and after calcination (green) from three batch

2.2. Synthesis of ZnO NPS

ZnO NPs of S,P,M and A are synthesized through facile sol-gel process. Typically, at first 4.36g ZAD was dissolved in a three-neck flask containing 360 ml of $_dH_2O$ to form a homogenous precursor solution. Now 40 ml of *S. cumini,* leaf extract (from refrigerated stock solution), was taken and drop wise added into the simultaneously with constant stirring, using magnetic stirrer, which results in visual color changes from colorless to dark greenish brown. Now the resultant

solution (0.04M) was set for reflex-heating at 80°C for 10 h at 1200 rpm. After a 10h, reflex-heating was turned-off and the solution was allowed to cool at room temperature for 8 h. The brown color paste was washed three times with *d.*H_2O followed by ethyl alcohol to eradicate associated soluble impurities and then placed into the oven at 60°C for 50 min to dry the precipitate. Eventually, the dried solid crystals were transferred in to crucible, wrapped with aluminum foil and put into a muffle furnace for calcination at 400°C for 2 h to obtain pure and crystalline NPs. Afterward calcined samples were grinded by using mortar and pestle to get dark brown color fine crystal of ZnO NPs of *S. cumini* [54]. Similar procedure is applied to synthesised ZnO NPs of *P. guajava, M. oleifera and A. indica*, and *represented* P, M and A, for characterization and study of comparative dye mineralization performance. Fig.2(a).revealed the steps involved in the green synthesis of ZnO NPs by utilising leaves extract of all four-plant S, P, M and A [55-62,67], whereas effect of nature of phytochemical on efficiency of reaction follow the order *P. guajava* > *S. cumini*> *M. oleifera* > *A. indica* which can be as concluded in Table.3 and shown by bar diagram, Fig.2(b).

Table 3. Illustration of percent (%) Yield of ZnO NPs

Sample Code of ZnO NPs	Batch wise obtained wt. of ZnO complex	Mean wt. of ZnO complex.	% Yield of ZnO Complex	wt. ZnO complex. before calcination from two different batch	Wt. ZnO NPs after calcination	% yield of ZnO NPs
S	0.4975	0.5133	11.77	2.2565	1.452	64.38
	0.5304					
	0.5121					
P	0.5694	0.7049	16.167	5.0648	3.682	72.69
	0.5894					
	0.9560					
M	0.1589	0.4469	10.25	1.2554	0.753	60.05
	0.1405					
	0.14805					
A	0.1723	0.1636	3.75	1.1746	.6534	55.62
	0.1501					
	0.1685					

2.3. Phytoconstituents screening and mechanism of formation of ZnO NS

Aqueous leaf extract of *S. cumini* [64], *P. guajava* [65], *M. oleifera* [66] and *A. indica* [68] has a rich array of bioactive phytoconstituents (secondary metabolite), as detailed in Table 2. Notably, flavonoids (Myricetin, Quercetin), tannins (Ellagic acid) and with hydroxyl (-OH) in polyphenolic gallic acid and carboxyl (-COOH) groups in caffeic acid serve as effective reducing agents and donate electrons (e^-) to Zn^{2+}, enabling their reduction to Zn^0 during green synthesis of ZnO NS, thereby influencing the kinetics of nucleation growth and enhancing stabilisation through chelation, thus preventing agglomeration [67-69]. A part from reduction of metal ion, above functional group moieties double as capping agents, modulating kinetics of nucleation growth and enhancing stabilisation through chelation in aqueous media, thus inhibiting agglomeration. Moreover, present

benzenoid and non-benzenoid ring in polyphenols and flavonoids, tannins trigger π-π stacking interactions with the zinc oxide surface, further bolstering nanostructure stability.

Table 2. Specific phytoconstituents screening in aqueous leaves extract of investigated plants [17, 62-68]

Active Phytochemical	Name of test/Reagents	Results	Interferences with respect to 4± ml Leaves extract of *			
			S. cumini	*P. guajava*	*M. oleifera*	*A. indica*
Alkaloids	Dragendroff's	Orange-red ppt	+	++	++	++
	Mayer's test	Creamy ppt	+	+	+	++
Carbohydrates	5 ml Fehling solution	Reddish brown ppt	++	++	++	++
	Molish's Test	Brown-violet ring	+	+	+	+
Glycoside	5% $FeCl_3$, Glacial AcOH, 50% H_2SO_4	Blue colour in junction of AcOH layer	++	++	+++	++
Flavonoids	10% $(CH_3COO)Pb$	Yellow ppt	+	+	++	+
	5% NaOH, 10% dil. HCl	Yellow to colourless	+	+	+	+
Saponins	Froth Test.	20ml distilled H_2O	+	+	+	++
Polyphenolic Tannins	5% $FeCl_3$	Violet -green color	+	++	+	+
	Braymer's (Br_2 (aq.)	Yellow to colorless	+	++	+	+
Basalms	90%C_2H_5OH, $FeCl_3$	Rose pink color	++	++	+	-

* - =Negative interference, += Poor interferences, ++**=Strong interferences

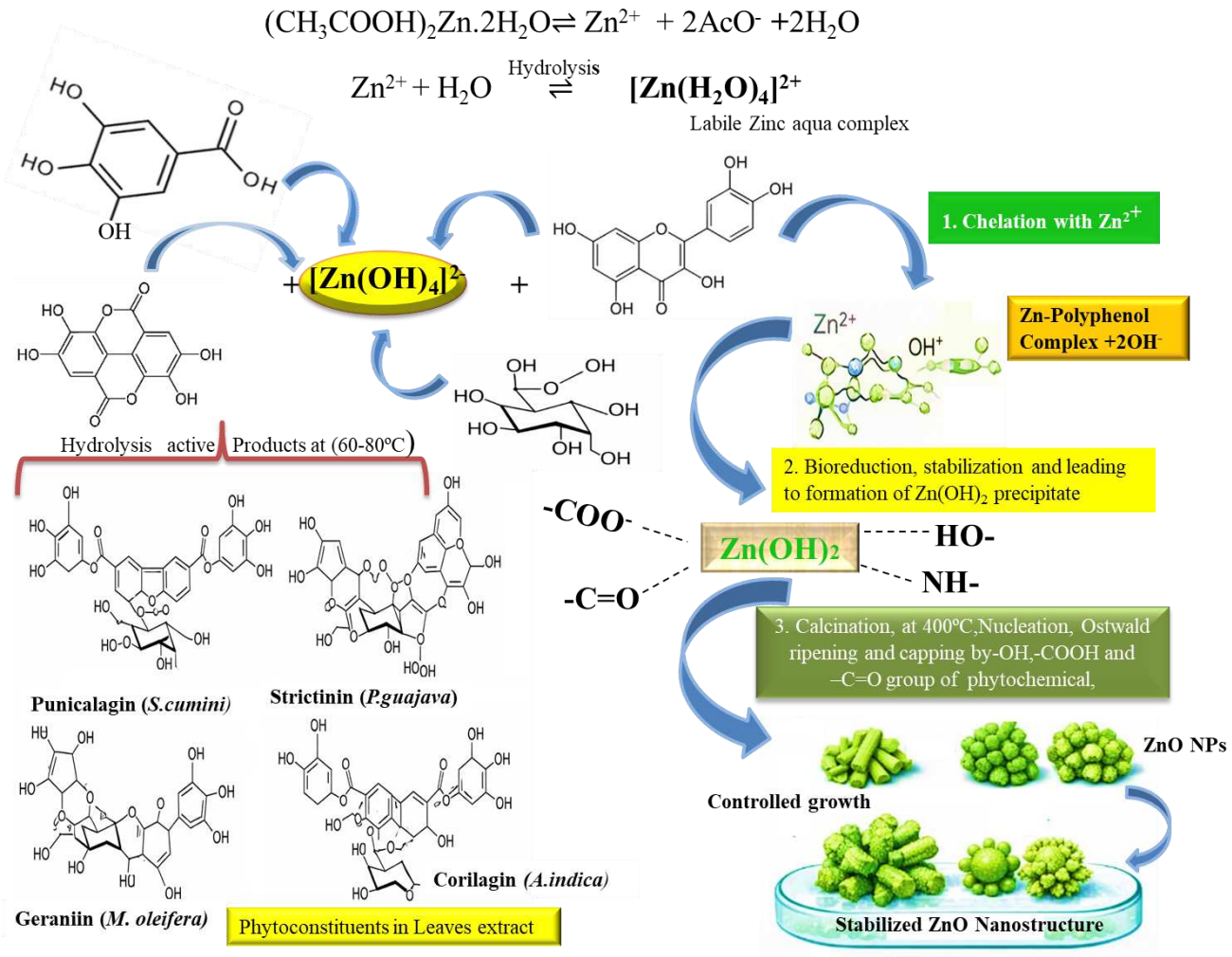


Fig. 3. Probable mechanism of reactions for Synthesis of ZnO NS sample using leaves extracts. [18, 32,45-46,61,63,68,70]

2.4. Qualitative and Quantitative Instrumentation

XRD, (Rigaku Miniflex300/600, Cu kα radiation, λ= 1.54178A˚, scan rate 4.00 °/min, step depth 0.01°, 2θ range 20°-70°) is used to evaluate the crystal structure, the crystallization level, and crystal phase of the ZnO NS. FTIR, (Bruker Alpha II) was fixed between 450 to 4000 cm^{-1} (wave number) for detection of essential functional groups (FG) present in extract (responsible for reducing, stabilising and capping), complex (before calcination) and ZnO NPs (after calcination). The Surface morphological, topological as well as elemental mapping and elemental overlay was examined by FESEM (Jeol JSM 7100F, Japan), coupled with EDX. DRS, (Lambda 750L1306253 PerkinElmer UV Win Lab 6.0.4.0738 / 1.61.00 Lambda 900) was used to measure the reflectance between 200 to 800 nm for the determination of the optical band gap energy (OBGE), of ZnO NPs. Along with above Dynamic light scattering (DLS, Malvern-ZS Ltd.UK) is used to measure zeta potential (ZP) and diameter of ZnO NS. Before determination of HDD, and ZP sample were dispersed in $_dH_2O$ {dielectric constant (78.5), refractive index (1.330), and viscosity (0.8872)} in disposable micro cuvette (40µl), subjected to probe sonicated for 1 min to ensure a homogenous suspension at controlled temperature of 25 °C. PL (PL, JASCO, FP-6500 Japan apparatus) spectra of ZnO NPs in were recorded at excitation wavelength of 350 nm at room temperature. UV-visible (Uv-1700 spectrometer) is applied to record the absorbance of degraded dyes sample at each 20 min of time interval.

2.5. Dye Mineralization Process.

For the open visible light (VL) photocatalytic reaction, MB, MG, BCB, RhB, EY and CR are selected as model pollutants. Stock aqueous solutions of each pollutant having a concentration of 10 ppm (0.01 g/1000 mL, with $_dH_2O$ (deionized water) acting as a solvent) was prepared in a conical flask. Subsequently, 0.1 g of ZnO NPs (S, P, M and A) was dispersed in 100 mL of 10 ppm dye solution (each time). Prior to illumination in sunlight (radiation ,4.35kwh/m^2d)[38], the dye suspension (having a photocatalyst) was stirred in the dark for 30 min using a magnetic stirrer to establish adsorption-desorption equilibrium (⇌) at room temperature. Aliquots (5 mL) were sampled every 20 min over 120 min (0=120 mins), and optical absorption spectra were recorded using a UV/Vis spectrophotometer, removing suspended photocatalyst particles by centrifugation (4000 rpm,5min ±).

3.Result and Discussion

3.1 XRD

The crystalline characteristics of the Phytofabricated ZnO NPs specimen were examined using XRD as illustrated in Fig.4(a-b). From Fig 4(a) was observed that the XRD pattern of the ZnO complex (before calcination) exhibited a noisy background without any clearly defined diffraction

peaks. The diffraction pattern exhibits distinct reflections at 2θ values of 31.979°, 34.795°, 36.448°, 47.762, 56.825°, and 62.980°, in S, P M and A sample, which are indexed to the (100), (002), (101), (102), (422), (110), and (103) lattice planes, respectively as shown in Fig.4(b)[20,22-24]. In sample S one peak appear at 2θ=67.120° which was indexed (200). Similarly in sample P, M and A one peak appear 2θ=67.87° that correspond to the (112) lattice plane. A slight shift in the diffraction peaks was observed, suggesting lattice modulation induced by plant extract (phytochemical variation) during nucleation and growth. These reflections confirm the formation of a well-crystallized, hexagonal wurtzite ZnO phase and close correspondence with standard reference data (JCPDS No. 03-065-3411), without detectable secondary phases, indicating that the plant extract does not alter the basic crystal structure during green synthesis [30-33]. The instrumental broadening was corrected using the instrumental FWHM value (~0.2°) obtained from the diffractometer specification. The true peak broadening was calculated using Eq. (1)[18].

$$\beta = \sqrt{(\beta_{(obs^2)} - \beta_{(inst.)^2})} \quad (1)$$

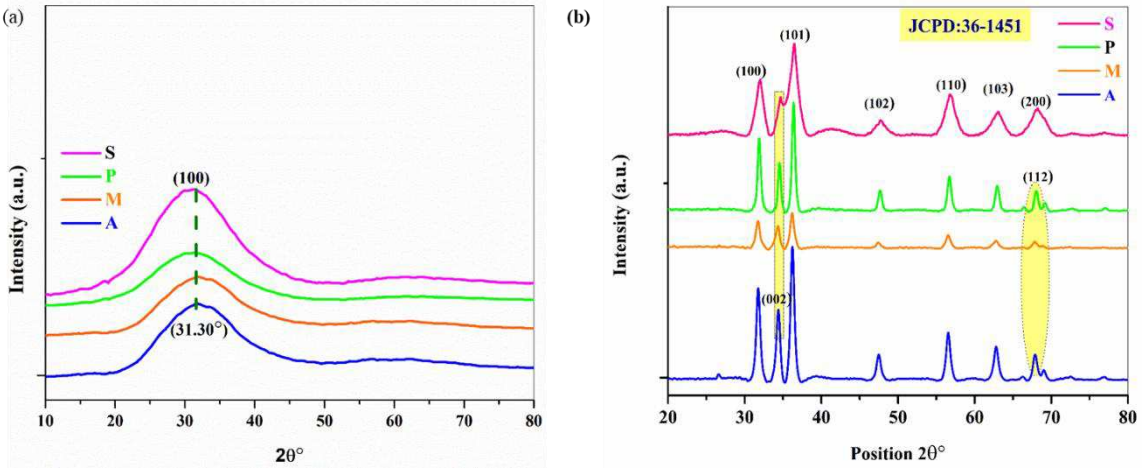


Fig. 4 XRD spectra of sample (a) before calcination ZnO complex and (b) after calcination, ZnO NPs

Corrected values were used for the calculation of interplanar distance (d) and crystallite size using Bragg's law (nλ=2dsinθ) and the classical Scherrer equation {D=(0.9λ)/(βcosθ)} respectively [34-36]. Similarly, microstrain (ε= βcosθ/4) from XRD peak broadening, the density of crystallographic defects (dislocation density =1/D²), and structural parameters (lattice constants a and c), calculated using the hexagonal structure equations mentioned in [44,61] from the first five prominent diffraction peaks to minimize peak-specific errors, were estimated, and the details are shown in table S1, whereas the mean values have been summarized in table 3 of four samples of ZnO NS. The calculated interplanar spacing (d) values were found to be in good agreement with standard ZnO values [43-44]. Slight systematic variation in d values across the samples, suggesting lattice distortion due to mismatch of ionic radius between Zn^{2+} and the dopant metal ions [55-63].

The FWHM values are systematically varied by concentration of dopant values, which implies variation in crystallite size and microstrain. The FWHM of the (002) peak progressively decreases for sample S (7.446°) and increases for sample (S<M<A<P). A slight broadening for sample S, compare to P, M, A suggests the introduction of lattice disorder implying enhanced peak broadening after doping, due to moderate variation in phytoconstituents (as shown in Table.S1).

Table. 3. Structural parameter of syntheised ZnO NS [a]

Sample	Average of first Five prominent peak {(100), (002), (102), (110), and (103)}					Lattice constant (Å)		
	Interplanar spacing (Å)	crystalline size, D (nm)		Microstrain ε ($x10^{-3}$)	Dislocation density ($x10^{-3}$ nm^{-2}	a	c (002)	c/a
		Scherrer Formula	W-H plot					
S	2.27±0. 0.47	6.668 ±0.646	14.0±2	14.5 ± 2.1	23.10±4.21	3.23±0.01	5.16±0.02	1.597
P	2.282 ± 0.479	16.93 ±1.693	14.0±2	5.21 ± 1.05	3.56 ± 0.64	3.23±0.006	5.18±0.012	1.069
M	2.286 ± 0.475	12.673±0.732	12.27±1.83	7.39 ± 1.82	6.27 ± 0.68	3.250± 0.004	5.19±0.012	1.064
A	2.291 ± 0.477	13.767±0.347	14.35±0.91	6.66 ± 1.40	5.26 ± 0.26	3.256±0.0028	5.22±0.013	1.603

a= Values represent mean ± standard deviation

The mean crystallite size, was estimated using the Debye–Scherrer approach, for sample S (6.668 ±0.646 nm) is less than sample M<A<P.

Addition to this the Williamson–Hall Plot was performed to estimate size, using the relation and shown in Fig.S1

$$\beta\cos\theta = (k\lambda/D) + 4\varepsilon\sin\theta \quad (2)$$

where ε represents the microstrain and D is the crystallite size

The W-H plot method given higher values of size for sample S (14.0±2 nm) due to the inclusion of strain contribution in peak broadening. The results from both methods were supports the reliability of the analysis.

Table.4. Comparative study volume and no of unit cell, average size (FESEM and DLS method), and zetapotential [a]

ZnO Ns Sample	Unit cell volume $(Å)^3$	No of unit cell ($x10^3$)	(101/002) Intensity ratio	Average Diameter of 50 particle (nm) From FESEM	Size distribution Hydrodynamic (DLS) method	Zetapotential (meV)
S	46.06 ±0.33	6.43±1.92	2.397	21.31	461.4	-23.7
P	47.09 ±0.22	103±0.31	2.24	108	603.9	-28.1
M	47.52 ± 0.16	42.7±0.76	1.584	19.17	518.9	-24.3
A	47.94± 0.15	54.4±0.42	1.899	19.01	276.7	-28.6

a =Values represent mean ± standard deviation

Sample P exhibited the lowest dislocation density ($3.56 \pm 0.64 \times 10^{-3}$), whereas sample S indicated a significantly higher value ($23.10 \pm 4.21 \times 10^{-3}$) and overall order is P<A<M<S.The average microstrain (AMS) trend tends to follow the change in the δ. The AMS increased from sample P <A<M<S, with sample P showing the lowest strain ($5.21 \pm 1.05 \times 10^{-3}$ nm^{-2}) and sample S exhibiting the highest value ($14.5 \pm 2.1 \times 10^{-3}$). This observation concludes with the fact that sample S (~6.668 ±0.646nm) with a smaller crystal size exhibited a relatively higher DD and MS of defects showing

more residual stress in the crystal lattice of ZnO NPs derived from *S. cumini.* The calculated lattice constants were found to be in order of a = 3.2± Å and c = 5.1±Å (α = 90°, γ = 120°) [18]. A slight variation in lattice constants was observed from sample S to A confirming substitutional incorporation of phytoconstituents into the ZnO lattice. However, the c/a ratio remained close to the standard value of ZnO (~1.602), indicating that the hexagonal symmetry is maintained despite of doping. The unit cell volume (UCV) and number of unit cells (*NOUC*) per crystallite (*n*) for ZnO NS samples were calculated, using following eq. (3) and (4) and error propagation was performed considering uncertainties in crystallite size and unit cell volume.

$$V=0.866\ a^2c \quad (3)$$

$$\text{NUC, } n = D^3/V_c \quad (4)$$

where a ,c D, and Vc are the calculated lattice constant (in Å), average coherent domain size (nm) determined from Scherrer equation and volume of unit cell (nm) respectively.

There was a slight variation in the unit cell volume (UCV) from (47.94± 0.15 to 46.06±0.33(Å)^3) which was observed changes in lattice constants (as tabulated in Table 4). Moreover, estimated value of NOUC per crystallite showing that the size of the crystallite decreased, the numbers of unit cells from sample P to S follow decreasing order, as P>A>M>S

The gradual change in the ratio of intensities (101/002), which is of the order A < M < P<S. The same progressive growth is reflected in the values of the microstrain with strain taking the order of P < A < M < S. The sample S with the greatest strain and DD also demonstrates the greatest intensity ratio, lowest unit cell volume (46.06±0.33Å) and number unit Cell (3.4±0.31x10^2) which indicates that the greater the distortion of the lattice the less the preferential growth that occurs along the (002) plane and enhance the contribution of the (101) plane. Since the internal stress of the particle due to variation in phytoconstituents has the propensity to augment lattice distortion, form the anisotropic crystal growth, and hence the reduced in c-axis orientation. In contrast to this, sample P with lower strain exhibits comparatively stronger (002) plane alignment. The observed variation confirms that peak broadening in sample S is the result of both structural imperfections and lattice distortion suggests non-uniform strain distribution within the lattice, which varies depending on the doping of phytochemical. The fact that the standard deviation (SD) of samples S and M is comparatively larger than that of samples P and A implies that the distribution of strains is not entirely uniform over the crystal planes. In contrast to this sample P has a lower strain and DD and SD, which could be attributed to better defect stabilization under the same synthesis conditions. This implies that the distortion of the resultant in the lattice is a major factor that determines the formation of texture in the process of Phyto-fabrication. The findings indicate that plane alignment

of lattice constant c has a strong correlation with internal strain and interstitial defects, but is not entirely determined by the crystalline size.

3.2 Functional group studies

The FTIR spectroscopy was conducted to examine the chemical functionality of phytoconstituents (stabilising and reducing) present in the plant extract, and their mechanistic role in NP synthesis is displayed, Fig. 4(a) between 400 and 4000 cm^{-1}. The plant extract showed a wide band at 3294-3340, which was associated with the O-H and N-H vibration and revealed the presence of polyphenolic, -NH_2(amines) groups [31-34]. The stretching >C=O (carbonyl) and >C=C< (stretching aromatic) absorption peaks at 1634-1734 cm^{-1} were attributed to the presence of flavonoid, tannins and other bioactive compounds. Bands near 988–1222 cm^{-1} correspond to C-H stretching, -COH, and >C=N vibrations of polysaccharides and phenolic constituents. Other stretching bands around 567-583 cm^{-1} were related to C-H and >C=C< [55-57,68]. After forming the ZnO complex (Fig. 4b) and the ZnO NPs after calcination (Fig. 4c), significant shifts of peaks and intensity reductions were recorded, which were related to the integration of -COOH, -OH, and -NH_2 in the reduction of the Zn^{2+} ion, influencing the nucleation kinetics, crystalline size, microstructural formation, and surface coordination. Importantly, the appearance of a characteristic absorption band in the 425–500 cm^{-1} region confirms Zn–O stretching vibrations, verifying the successful formation of ZnO NPs [52].

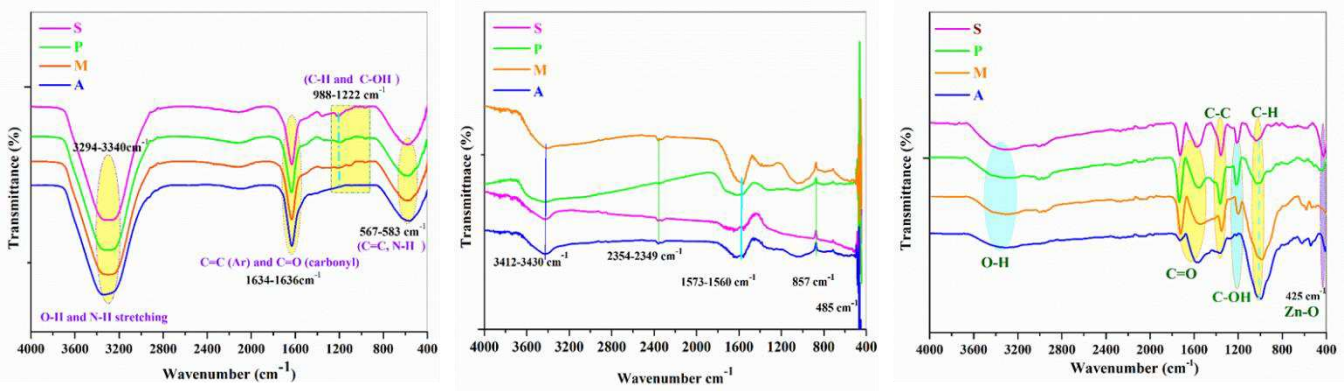


Fig.5 FTIR analysis of (a) Extracts (b) ZnO Complex before calcination (c) ZnO NPs after calcination

3.3 Optoelectronic studies

In photocatalytic reactions, band gap energy (*Eg*) plays a key role, as the photocatalyst (a semiconductor) requires light with energy equal to or exceeding photon energy to activate. All ZnO NP samples showed strong UV absorbance below 380 nm, typical of ZnO's wurtzite structure. This indicates the absorption edge corresponds to the intrinsic band-gap (BG) transition of ZnO arising electron excitation from the O_{2p}-dominated valence band (VB) to the Zn_{4s}-dominated conduction

band (CB) [19-23]. Fig. 5(a) shows the direct OPBGE values of ZnO NS were obtained from the Tauc plot of versus by extrapolating the linear segment to the photon energy axis and used to estimate CB and VB, systematically organize in Table.6 The resulting S, P, M and A values are 2.90, 2.66, 2.74 and 2.92 eV, which are less than standard ZnO values (~3.10± eV). This observation indicates that phytoconstituents are associated with the ZnO lattice. Moreover, the samples P and M displayed quite similar values, with a slight increase for samples S and A due to smaller particle size (Table 4), which causes slight rises in OPBGE (Eg) value [23].

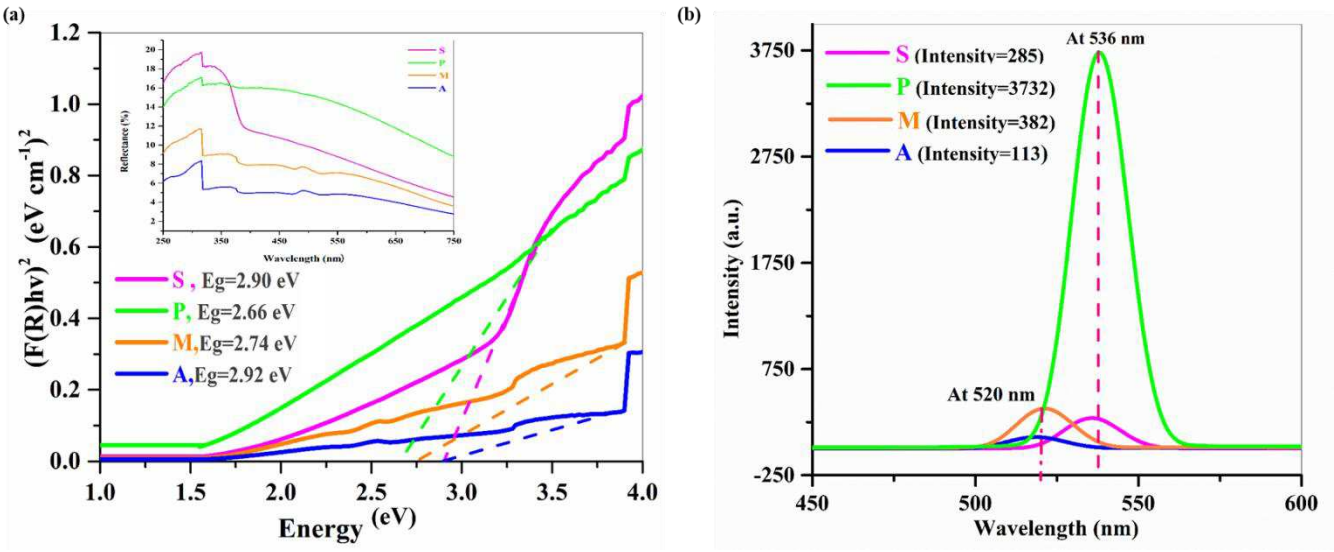


Fig. 6 (a) UV–Vis DRS (inset) along with the Kubelka–Munk (K-M) function vs photon energy ((*hv*) to determine the direct OPGE of ZnO NS (b) RTPL of ZnO NS

Study of room-temperature photoluminescence (RTPL) quenching of semiconductor material ZnO NPS between 350 and 600 nm provides critical insights about photocatalytic quantum yield (Φ). For efficient visible light photodegradation, the radiative recombination of photogenerated carriers represented by the PL emission must be minimised to allow surface photochemical reactions, as illustrated in Fig. 6(b). ZnO NS (A and M) exhibit distinct broad emission centered at 520 nm with reduced intensity (113 and 381). Similarly, NPs obtained from *S. cumini* and *P. guajava* also show green emission at 536 nm (visible region) with 285 and 3732 a.u. intensity, respectively. This visible luminescence is attributed to vacancies of oxygen (VO) and zinc (V_{Zn}) and evidence for the solar-light-active (SLA) nature of the photocatalyst [24]. These intrinsic defects in the lattice of the S, P, M and A photocatalyst create sub-bandgap states that promote the absorption of photons with lower energy, act as trap sites for e^-, and reduce immediate e^-/h^+ recombination in the VB [25]. Pudukudy *et al.* [30] also reported that emission at 554 and 617 nm originated from surface defects or vacancies of single oxygen (~ 0.21 eV or above the VBM). This correlation confirms that the lattice defects (especially VO) within the ZnO NS are not merely structural flaws but are the primary drivers for the generation of reactive oxygen species (ROS), such as the hydroxy free radical (•OH) and superoxide free radical ($O_2^{\bullet-}$) under visible light irradiation [33]. These ROS play

a significant role for surface-catalysed redox reactions between adsorbed organic pollutants **(**dye molecules) on active sites and H_2O [44, 45, 47, 52].

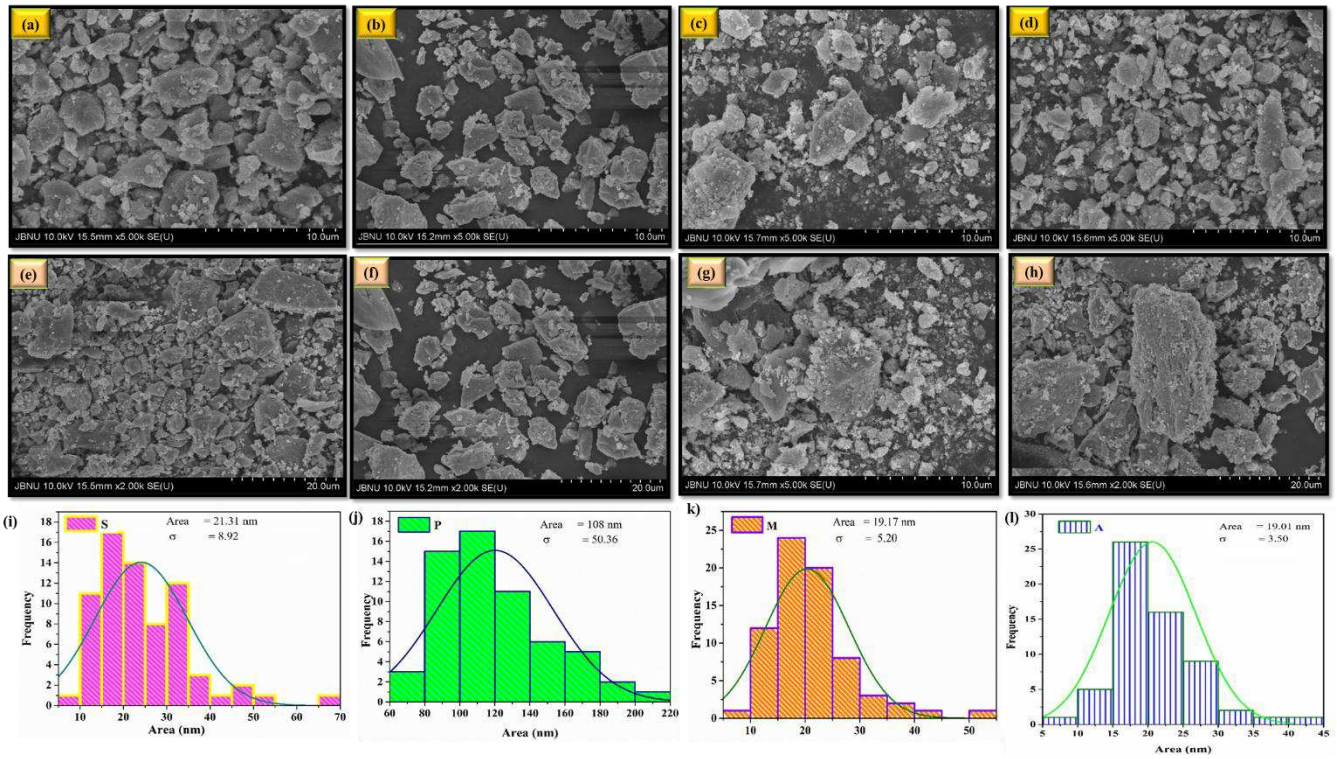


Fig.7 FESEM image (a-d)10 µm (e-h) 20 µm, and (i-l) Histogram of Particle size data from FESEM measurements were performed using Image J 1.52a software for ZnO NS sample S, P, M and A respectively

3.4 Morphological, Particle Size and Colloidal Stability

FE-SEM along with DLS was used to examine the comprehensive morphological and size distribution of the synthesised ZnO NS sample. FESEM micrographs were illustrated at two different magnifications (Fig. 7 a-d, 10 µm) and (Fig.7 e-h, 20 µm). Micrographs of samples S, P and A show that they are irregular, flake-like with hierarchical aggregated particles with a high surface-volume ratio due to the rough surface [33-34,55]. Similarly, the topography of sample M revealed a fine crystalline size. Increase in temperature and synthesis time (~10 hrs.) may also favour aggregation of the nanoparticles, resulting in increased particle sizes [17-18]. This hierarchical aggregate suggests that the phytochemical like tannins function as efficient capping [63] and stabilising agents influence the nucleation and growth kinetics because of the reduction in surface free energy during biosynthesis process [18].Moreover, ImageJ software was used for analysis of FESEM micrographs, and average areas were found to be 21.31±8.92, 108±50.36, 19.17±5.17 and 19.01±3.50 nm for the S, P, M and A ZnO NS, respectively, as shown in Fig. 7 (i-l). The particle size histogram in Fig. 7(j) shows an average size of ~ 100 nm with an SD of 50.2 nm, indicating a broad particle size distribution in sample P.

The synthesis of ZnO NPs characterised by triangular-shaped morphology and an average size of 25.40 nm, utilising *Livistona chinensis* leaf extract and $ZnCl_2{\cdot}2H_2O$ as sources of Zn^{2+} ion [18].

Extracts derived from the peel of *H. polyrhizus* yielded nanoscale wurtzite hexagonal ZnO with a spherical shape and dimensions ranging from 56 nm [31]. Similarly, extracts of P. granatum, *C. phlomidis* (peel) [32-33], and H. sabdariffa (flower) [34] produce spherical, spherical and agglomerated particles, averaging ~10-45, 40-60 and 8.71-38.63 nm in size. Likewise, an eco-friendly, non-toxic approach, utilising S. *cumini, P. guajava, M. oleifera and A. indica* leaf extracts, yields ZnO NPs with agglomerated [55], semi-spherical [57], spherical [58], flower-like [59], and flaky-to-spherical [61, 63] morphologies in the 10-68 nm range, respectively. Certainly, variations in morphology and size (dimension) differences have been reported in the plant-mediated synthesis of ZnO NPs using plant extracts of *Garcinia cambogia (fruit),* ***Salvia officinalis (leaf)****, etc.,* and the results were tabulated in Table .7 [35-54].

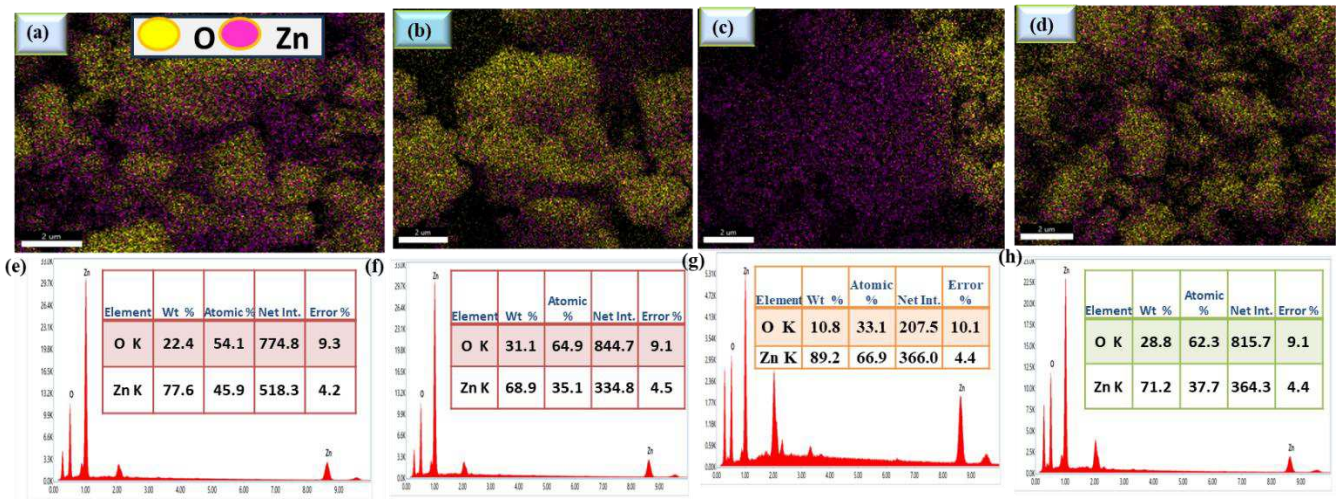


Fig.8 Elemental overlay (a-d) and, EDX spectra along with elemental composition graph (e-h) for ZnO NS sample S, P, M and A respectively

The elemental composition and high purity of the synthesised ZnO NS were confirmed by the EDX spectroscopy. Fig. 8 (a-d) represents the elemental overlay of zinc (Zn) and oxygen (O) atoms present in samples S, P, M and A, respectively. Along with these signals of Zn and O, they were seen in Fig. 8 (e-h), and the weight percentage (wt%) of Zn and O was found to be about 77.6 and 22.4%; for S, 68.9 and 31.1%; for P, 89.2 and 10.8%; and for M, 71.2 and 28.8%, without a detectable extra peak in all four samples, which is the evidence of the formation of phase-pure ZnO nanostructure. Similarly, the atomic % of Zn was found to be 45.9±4.2, 35.1±4.5, 66.9±4.4 and 37.7±4.4 for S, P, M and A ZnO Ns, respectively. The hydrodynamic diameter (HDS) reflecting the solvent-associated solute layer on ZnO NS was evaluated via DLS analysis [17]. The resultant distribution curve, Fig. 9(a-d)) showed that all four samples, S, P, M and A (RI and material absorption 1.59 and 0.010), exhibited a narrow intensity distribution centered at a mean HDD of 463, 603.9, 574.5 and 276.7 nm. The polydisperse index (PDI) values of ZnO NS are 0.327, 0.345, 0.318 and 0.285 with intercepts of 0.839, 0.851, 0.930 and 0.898 for the S, P, M and A ZnO NS,

respectively [19]. The lower value of polydisperse index (PDI) of sample M revealed its monodispersed phase and stable uniform clusters [33]. DLS measurement confirmed the bimodal size distributions of S and A with two peaks. Sample P and A was moderately polydisperse.

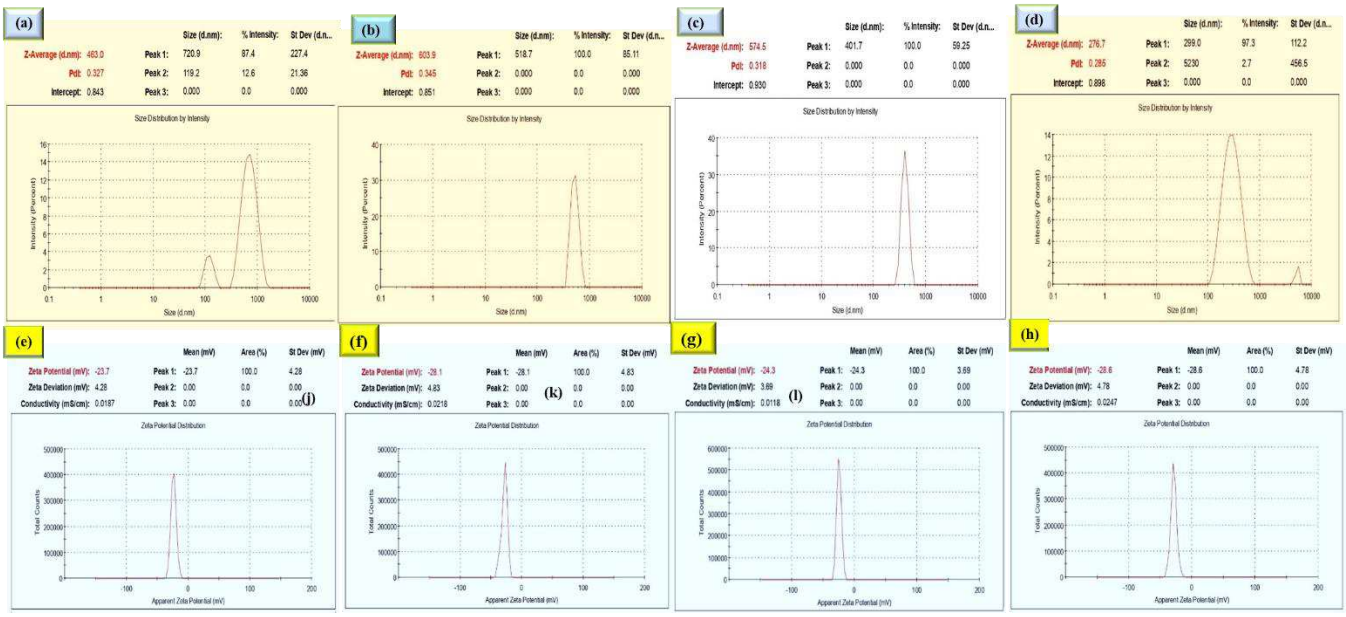


Fig.9 (a-d) Cumulative particle size distributions, (e-h) Zetapotential measured by DLS method over ZnO NS sample S, P, M and A respectively

It is important to note that the HDD measured via DLS and FESEM is inherently larger than the mean crystalline size calculated from XRD data based on SE, indicating the polycrystalline nature of the sample. XRD merely measures the core size of solid NPs [19, 33, 37], whereas FESEM identifies the overall dimension of particles that could have an assembly of multiple crystallites. This size disparity is also attributed to the adsorption of dH_2O and the non-homogenous distribution of ZnO NS in suspension during measurement of HDD. The use of both XRD and FESM thus gives a better insight into the structural and morphological features of the green-synthesised ZnO NS. Moreover, the HDD of green synthesised ZnO NS is larger than chemically synthesised ZnO-PP (147 nm) [23], suggesting that present phytochemicals within the aqueous leaf extract, adsorbed at the surface of NPs thus, hydrodynamic cell size may increase [50].

In addition to this, a study of ZP measurement was applied to assess the electrokinetic (EK) and colloidal stability (CS) of ZnO NS, and the results are displayed in Fig. 9(e-h). The recorded values of ZP in neutral medium (pH=7) were -23.7±4.28, -28.1±4.83, -24.3±3.69, and -28.6±4.78 mV with conductivity 0.0187, 0.0218, 0.0118, and 0.0247 mS/cm with respect to samples S, P, M, and A. This observed negative potential (ZP, ±20–30 mV) due to adsorbed polar -OH, $-NH_2$, functional group (polyphenols and flavonoids)present in leaf extract indicates sufficient repulsive forces to maintain a metastable colloidal state [33,36], balancing the van der Waals attractions to prevent

rapid agglomeration, and confirms the robust stability of ecofriendly ZnO NS in the aqueous system during photodegradation of pollutants [51,56,72].

3.5. Study of Photocatalytic response of dyes

The photocatalytic performance of the phytosynthesized ZnO NS (S, P, M and A) via cheap and nonhazardous route was evaluated against six dyes (MB, MG, BCB, Rb171, EY and CR) under ambient sunlight (35°C±). As the sun provides abundant, renewable solar energy particularly in India, it is ideal for advancing photocatalysis and Sustainable Development Goals (SDGs), underscoring the need for efficient solar-responsive photocatalysts. The photodegradation (PD) efficiency, degree of degradation (DD) of each NPs over dye, is calculated by applying the following Eq. (3), and Eq. (4) [29-31]. However, decomposition of cationic and anionic dye follows pseudo-first-order (PFO) kinetics. The apparent rate constants (K_{app}) for PD of pollutant by ZnO NPs were measured with the help of the Langmuir-Hinshelwood (L.H.) kinetics model as illustrated in Eq. (6) [32-33].

$$\text{PDE (\%)} = \left(\mathbf{1} - \frac{C_t}{C_0}\right) \times \mathbf{100} \quad \text{.... (4)}$$

$$DD = (\text{Ct/Co}) \quad \text{..... (5)}$$

$$\boldsymbol{ln\left(\frac{C_0}{C_t}\right) = kt} \quad \text{.... (6)}$$

Where, Co and Ct are the absorbance of dyes at t=0 and t=20-140 min of time interval,

3.5.1 Degradation of cationic, MB, MG BCB dyes.

Fig. 10(a-l) and illustrates time-dependent UV–vis spectra for MB, MG and BCB, revealing a progressive decrease in absorption maxima (λmax) over 0–120 min of open sunlight exposure (OSLE) with the ZnO NS. At t=0 min, (adsorption ⇌desorption) negligible photobleaching (<3±%) of the dyes was observed under dark conditions. This observation confirms substantiating the requisite photon energy for photoexcitation in activating charge carrier generation within the phytofabricated ZnO NS for dye mineralization. Karthik *et al*. reported that dyes solution without photocalyst shows negligible change in sunlight exposure [52,55]. Similarly, Suneel *et al*. [71] and Lim *et al*. [73] and also performed a control experiment showed minimal degradation (4.52–8.91%) by MB, Rb171, and RhB dye suspension containing composites in the dark, confirming sunlight as the primary driver for photocatalysis.

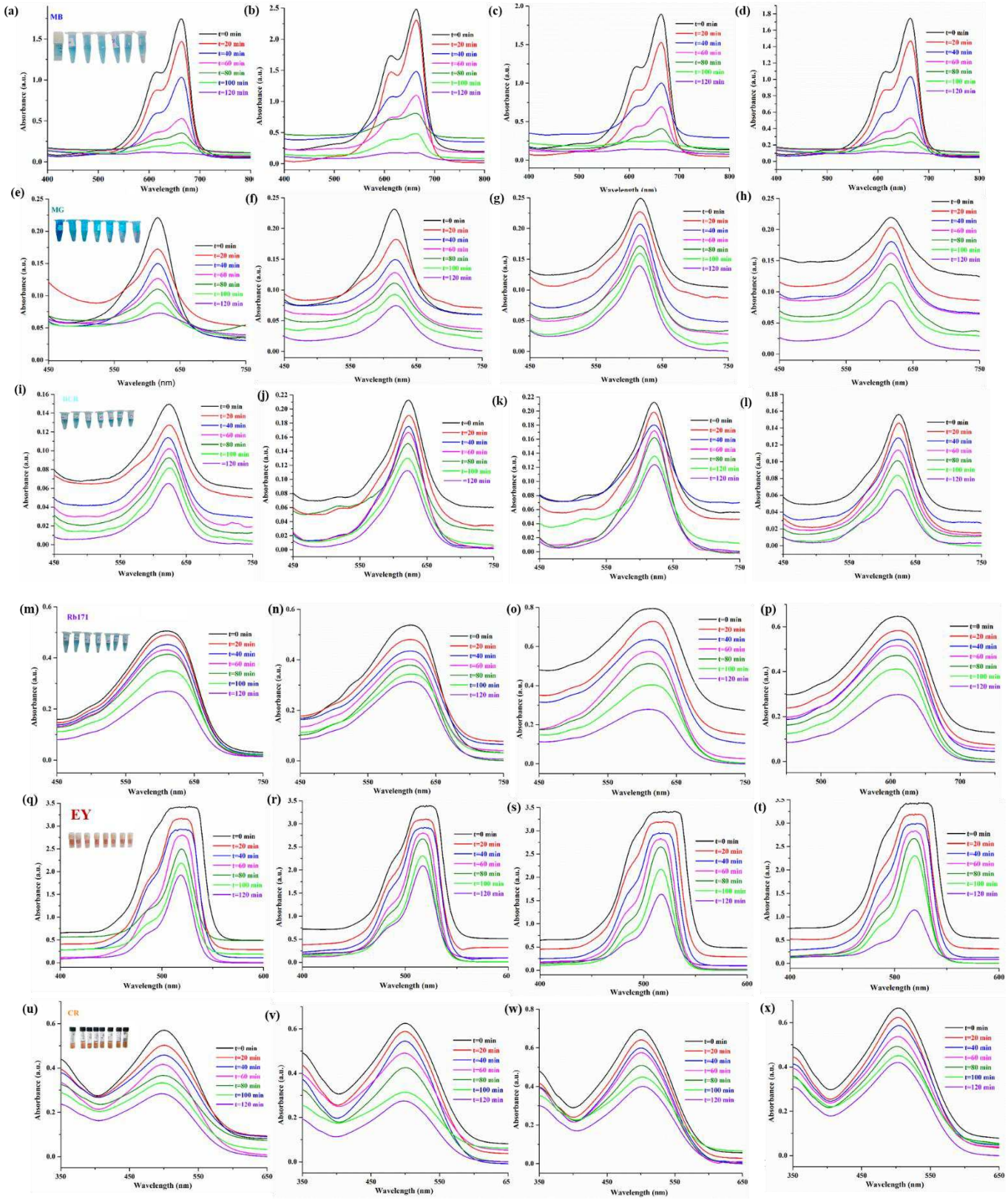


Fig.10.Illustration of Time dependent UV-vis absorption spectrum of (a-l), cationic MB, MG and BCB and (m-x) anionic Rb171,EY and CR dye suspension over ZnO NS sample S, P, M and A respectively

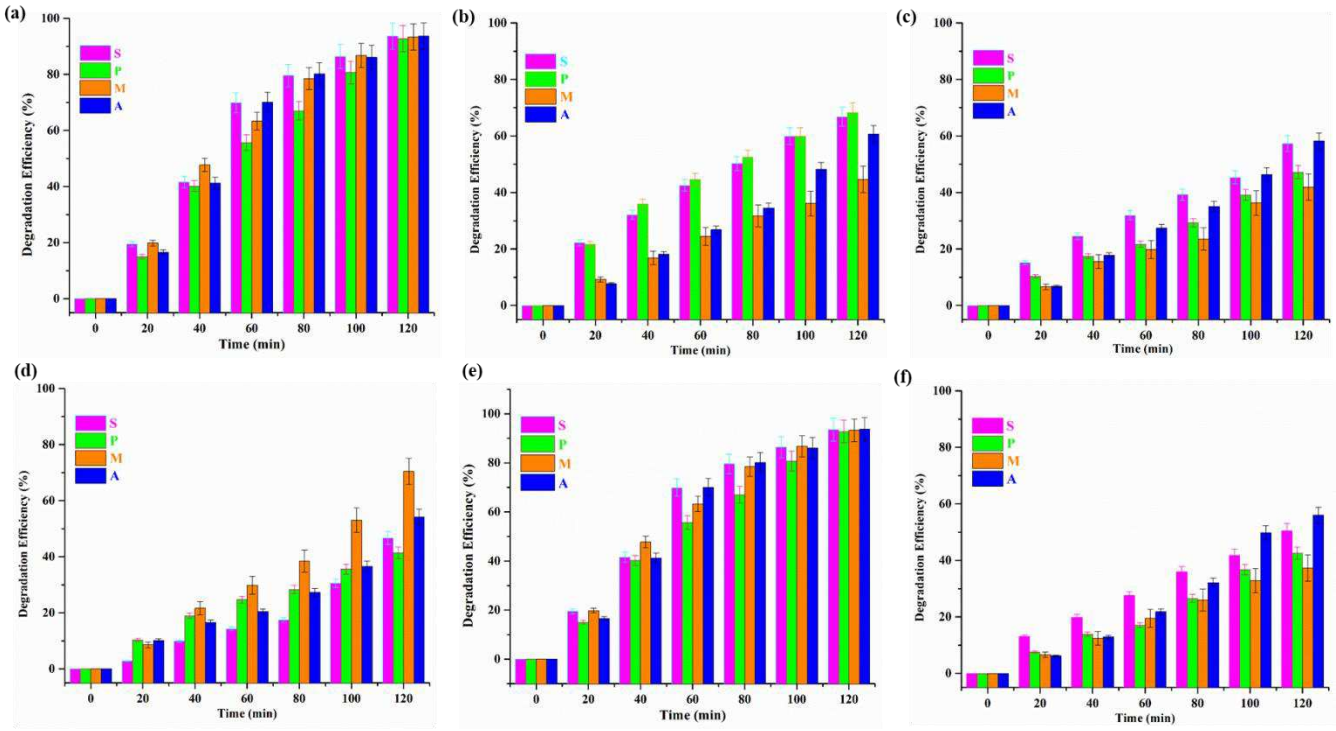


Fig.11 Illustration of degradation efficiency of ZnO NS sample S, P,M and A , over (a)MB , (b)MG,(c)BCB, (d)Rb171, (e) EY and (f) CR dye

As illustrated in bar diagram Fig. 11(c-d), S, P, M and A achieving approximately 93.6, 92.80, 93.28 and 93.71 % degradation for MB respectively. The MG mineralization percentage was found to be 66.83, 68.26, 44.57, and 60.72% for S, P, M and A, ZnO NS sample. Likewise, the BCB decolorization percentage was calculated to be 57.27, 47.16, 41.98 and 58.28% for S, P, M and A, respectively, within 20-140 min of OSL exposure. As illustrated from Fig.12 (a-c), upon OSL, irradiation, the extent of degradation (C/C_0) of all target dyes declines exponentially across S, P,M and A photocatalyst. Photocatalyst M demonstrated the lowest degradation efficiency, achieving approximately 44.57% and 41.98% mineralization for MG and BCB dyes, respectively, in 140 min OSLI. For MG and BCB dye, the PDE of Sample S is ~1.50 and 1.36 times higher compared to Sample M, attributed to a monodispersed, uniform and smooth surface with less negative ζ (-24. 3) ZnO NS derived from *M. oleifera.* The photocatalytic and kinetic parameter corresponding to all synthesized ZnO NS presented in Table.5

Table 5. Photodegradation performance of ZnO nanostructure derived from S, P, M and A, exposure to 120 min of open sunlight

Photocatalytic and				Kinetics Parameter		
Model Pollutants (dye)	Nanomaterial (sample)	Conc of dyes and its Volume	Degradation efficiency (%)	K_{app} (min^{-1})	Half-life ($t_{1/2}$) min	Regression coefficient ($R^{2)}$
MB	S		93.60	0.0252	27.50	0.98942
	P		92.80	0.0204	33.96	0.96166
	M		93.28	0.0024	30.86	0.99062
	A		93.71	0.0231	30.94	0.98853
MG	S		66.83	0.0088	78.75	0.99745
	P		68.26	0.0090	77.0	0.99692
	M		44.57,	0.0048	144.38	0.99776
	A		60.72	0.0075	92.4	0.97471
	S		57.27	0.00651	106.48	0.99072
	P		47.16	0.00508	136.45	0.9883

BCB	M	10 ppm, 100mL	41.98	0.00446	155.42	0.98367
	A		58.28	0.00708	97.90	0.9831
Rb171	S		46.74	0.00474	146.20	0.92729
	P		41.38	0.00428	161.92	0.99695
	M		70.37	0.00807	85.87	0.96279
	A		54.16	0.00567	122.2	0.9466
EY	S		43.72	0.00472	146.8	0.99673
	P		38.52	0.00382	181.5	0.98503
	M		52.19	0.00551	125.8	0.99823
	A		66.47	0.00506	136.9	0.96907
CR	S		50.52	0.0056	123.78	0.98555
	P		42.58	0.0046	150.69	0.98211
	M		37.33	0.0039	177.74	0.9369
	A		56.07	0.0071	97.63	0.9397

3.5.2 Degradation of Anionic dyes.

Time-dependent UV-vis. characteristic absorption maxima of Rb171 (615±nm), EY (518±nm) and CR (499±nm) were continuously monitored as a function of irradiation time to quantify photodegradation kinetics for dye suspension. From Fig. 10(m-x), it was observed that the intensity of the peak decreased with an increase in exposure time from, t=0-120 min. The bar diagram, Fig. 11(e-f) demonstrates that ZnO NS, M achieves 70.36% (Rb171), and a mineralized 66.46% (EY) chromophore decolorization within 120 min of OSLI. To elucidate shape, size and phytoconstituent quenching-dependent photocatalytic performance, normalized concentration (C/C_0) profiles for Rb71, EY and CR degradation across S, P, M and A were designed, as illustrated in Fig. 13(e-f). After 140 min OSLE, DE of ZnO NS sample M (70.37%) > A (54.16%) > S (46.74%) > P (41.38%) over Rb171 dye. The EY mineralization % was found to be 66.47, 52.19, 43.72, and 38.52% for A, M, S, and P, respectively. In the same way the PDE was monitored, 56.07, 50.52, 42.58, and 37.33% for A, S, P, and M, respectively. Overall DE of sample A is found to be good over all three anionic dyes. Time-dependent UV-visible characteristic absorption maxima of Rb171 (615±nm), EY (518±nm) and CR (499±nm) were continuously monitored as a function of irradiation time to quantify photodegradation kinetics for dye suspension. From Fig. 10(m-x), it was observed that the intensity of the peak decreased with an increase in exposure time from t=0-120 min. Fig. 11(e-f) demonstrates that ZnO NS, M achieves 70.36% (Rb171), and a mineralized 66.46% (EY) chromophore decolorization within 120 min of OSLI. To elucidate shape, size and phytoconstituent quenching-dependent photocatalytic performance, normalized concentration (C/C_0) profiles for Rb71, EY and CR degradation across S, P, M and A were designed, as illustrated in Fig. 13(e-f). After 120 min OSLE, DE of ZnO NS sample M (70.37%) > A (54.16%) > S (46.74%) > P (41.38%) over Rb171 dye. The EY mineralization % was found to be 66.47, 52.19, 43.72, and 38.52% for A, M, S, and P, respectively. In the same way the PDE was monitored, 56.07, 50.52, 42.58, and 37.33% for A, S, P, and M, respectively. Overall DE of sample A is found to be good over all three anionic dyes.

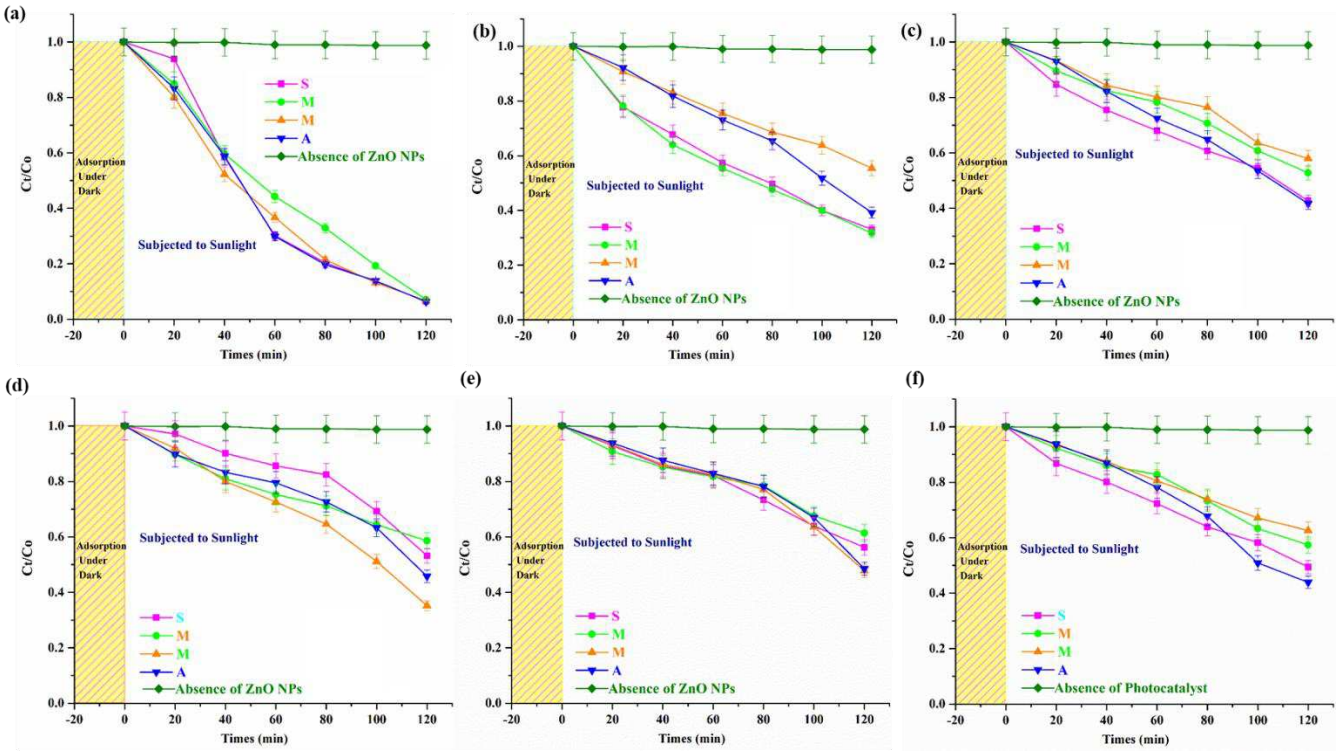


Fig.12 Illustration of degree of degradation of (a)MB, (b)MG, (c)BCB, (d)Rb171, (e) EY and (f) CR dye, over ZnO NS sample S, P, M and A

3.5.3 Kinetics of Photodegradation of Dyes

To evaluate the degradation kinetics of the basic and anionic dyes, the L-H kinetic model was applied. The K_{app} was derived from slope, via linear fitting of the ln(C0/C) vs irradiation times, and findings are displayed in Fig. 13(a-f) [61-63]. The summarized K_{app}, $t_{(0.5)}$ and correlation coefficients (R^2) results are illustrated in the table.5. From Fig. 14 (a-c), it was observed that the MB decreasing Kapp values for ZnO nanostructure S > A > M > A were 0.0252, 0.0231, 0.0224 and 0.02041 min^{-1}, respectively. In the case of Rhodamine MG, Kapp was found to be 0.0090 > 0.0088 > 0.0075 > 0.00477 min^{-1} for the P, S, A and M ZnO NS, respectively. For the BCB, K_{app} follows the order 0.0070 > 0.0065 > 0.00508 > 0.00446 min^{-1} for samples A, S, P and R, respectively.

Similarly, the bar diagram shown in Fig. 13 (e-f) displays the degradation of the K_{app} value of anionic dyes. For Rb171, the calculated K_{app} values (min^{-1}) for the ZnO NS sample were found to be M(0.00807)>A(0.00567) > S (0.00474) > P (0.00428). Likewise, the evaluated photodegradation K_{app} for EY dye was found to follow the order A (0.0071 min^{-1})>S(0.0056 min^{-1})>P (0.00461 min^{-1})>M (0.00398 min^{-1}), and for CR dye, M(0.00551)>A(0.00506)>S(0.00472)>P (0.00382 min^{-1}).

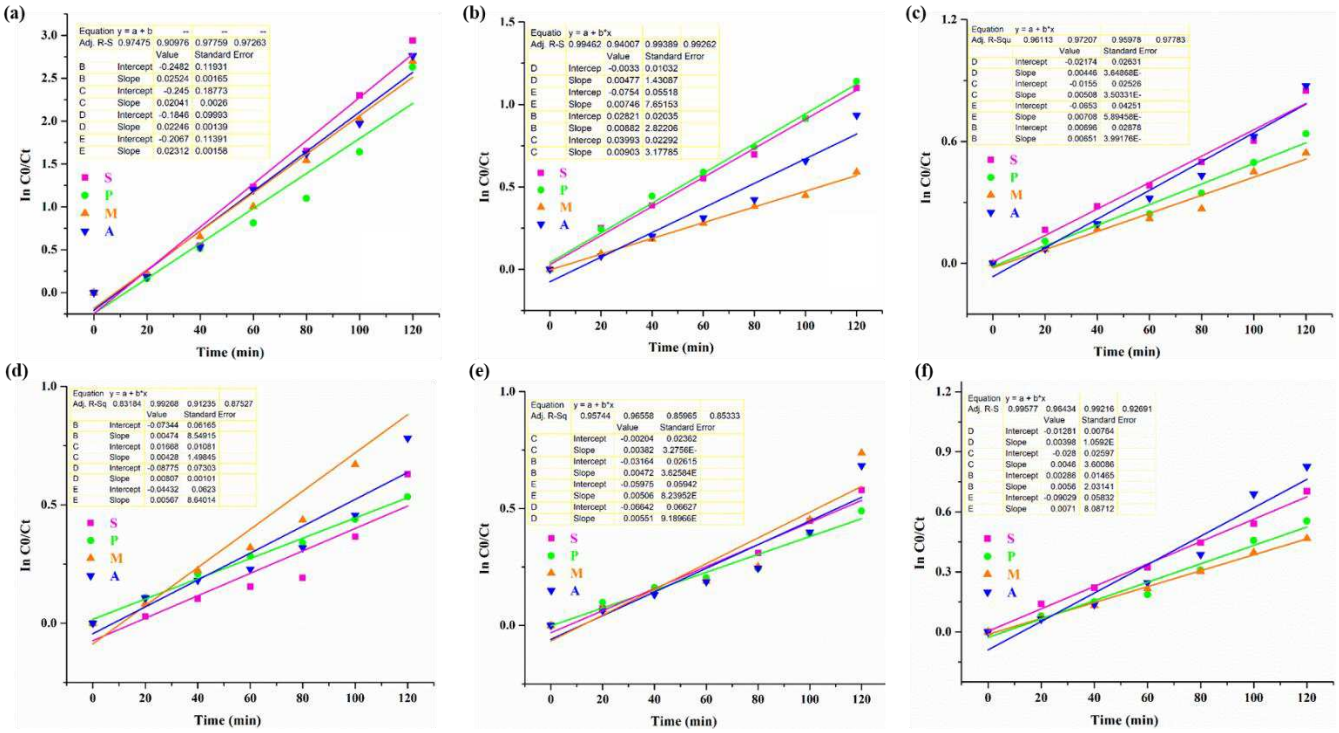


Fig.13 Illustration of Kinetics of degradation of ZnO NS sample S, P, M and A over (a)MB, (b)MG, (c)BCB, (d)Rb171, (e) EY and (f) CR dye, respectively

Notably, the sample S exhibits superior photocatalytic turnover frequencies (TOF) followed by P and A with respect to cationic MB, MG and BCB dye. On the other side sample A also exhibited good photodegradation over CR (66.47%)>EY(56.33%)>Rb171(54.16%). Similarly, chemically synthesized bare ZnO exhibited substantially lower efficiencies than the highlighting the pivotal role of phytochemical in ZnO NS formation in boosting activity [71].

Furthermore, since the PD process of the investigated dye follows the PFO kinetics model, the corresponding half-life was calculated ($t_{1/2}$=0.6932/K_{app}), tabulated in the table. 5 and used to further access the PCP of the synthesised ZnO NS sample. For MB, sample S exhibited the lowest half-life value (27.50 min), indicating accelerated degradation kinetics (DK) and enhanced PE. In contrast, MG degradation was most efficient over sample P, which showed the shortest time (77 min). For BCB, sample A demonstrated the fastest degradation activity with 97.90 min. Similarly, for the anionic dyes Rb171, CR, and EY, the minimum values were calculated as 85.87,97.63 and 125.80 min for samples M, A, and M, respectively, demonstrating their better PCP toward the respective dye molecules in the aqueous system. Additionally, the high correlation coefficients (R^2) ranging between 0.927 and 0.989± for almost all samples (presented in Table. 5) confirm the excellent fitting of the experimental data to the PFO kinetic model, thereby supporting good photocatalytic performance of the examined dye in OSLI.

This variation in PCP can be attributed to the synergy between its hierarchical morphology, rough surface and phytogenic surface functionalization, which collectively facilitate efficient

photogenerated charge separation and increase the number of ROS ($\bullet O_2^-$, $\bullet OH^-$) within ZnO nanodomains [52].These variation in DE and K_{app} and disparities also correlate inversely with PL quenching, and narrow OPBGE of samples S, P and A, facilitate extended exciton lifetimes and vis-NIR (750–1400 nm) solar light harvesting. Moreover, the negatively charged surface of the ZnO NS (-ζ) facilitates the adsorption of positively charged cationic dye molecules through electrostatic interaction, providing more active sites for photocatalytic reactions. The above finding shows a significant variation in the DE behavior depending on which mainly depends on both; one is structure of dye molecule, and the other is catalyst surface composition due to different functional group in phytoconstituents. Moreover, Table 7 illustrates the comparative studies of the photocatalytic potential of ZnO NS with previously reported literature for photodegradation of dye, polyhydrocarbon, antibiotics and other organically contaminated wastewater. Gnanaprakasam *et al.* [20] reported the effective UV-induced (400W lamp) 95 % and 75% photocatalytic degradation (PCD) of 100 mL of AR27 and CRFB dye having concentration 25 ppm in 120 and 60 min, using chemically synthesized TiO_2 as a semiconductor catalyst. Hairom *et al.* [25] reported that ZnO-PVP-St, synthesized via coprecipitation method using PVA, $H_2C_2O_4$ and $(CH_3COO)Zn.2H_2O$ as precursor of Zn^{2+}, showed 72 % photocatalytic activity (PCA) in 240 min, compared with ZnO NPs synthesized at low temperature through coprecipitation method, which degraded 80% CR in 120 min of UV light illumination [27]. Several studies have reported high degradation efficiencies of bio fabricated ZnO photocatalyst. Fouda *et al.* [32] synthesized Spherical shaped ZnO NPs using *Punica granatum* peel extract and evaluated its performance against 10ppm MB. After 210 min of UV irradiation, degradation efficiencies (DE) of,93.4 % was noticed. In comparison with these reports, the ZnO with 23.1nm diameter was synthesized at 70 °C using fruit extract of *Rubus coreanus*. Under 100w of Tungsten bulb, nearly 90% degradation of MG (10 ppm, 90 mL) was achieved within about 240 min using *0.005*g of *rice shaped* ZnO NPs. Davar *et al.* [41] synthesized spherical shaped ZnO NPs (3.21 eV) utilizing Lemon juice and 0.004 M ZAD and 0.012 mol $C_{12}H_{22}O_{11}$ and investigated photodegradation performance (PDF) using 25mLof MO (10ppm), MR (25ppm) and RB21 (20ppm,75mL) as model dye pollutants under 400W UV, irradiation, for 40 and 270 min respectively. Later on, morphology-controlled ZnO NS, have also devoted significant attention.

Table 5. Comparative catalytic performance of plant fabricated ZnO nanostructure with reported research

Photocatalyst size (nm) and shape	Source of Reducing / stabilizing, capping agent	Band gap (eV)	Pollutants & degradation (%)	Conc. of Pollutant /Volume of solution (mL)	Time (min)	Source of illumination	Kapp (min^{-1})	Half-life ($t_{1/2}$) min	Refer ence
Cu_2S, 17.77 nm Hexagonal	Chemical	3.13	RhB,53	5 ppm,50 mL	180	70W mercury lamp	0.0062	111.8	16
FeO-MNPs 16.5, spherical	*A. indica (leaf extract)*	3.27	RY176 95.18	30 ppm/L pH=4	250	500 W Xenon lamp	0.0212	3.26	17

α-Fe_2O_3,32.50 nm		2.25	MG, 68			Visible light	0.0109	63.59	
spherical	*Livistona chinensis*	2.98	MG, 79	10ppm,	90		0.0136	50.97	18
ZnO,37.50				100 mL					
triangular									
S	*S. cumuni*	2.90	MG,66.83	10ppm,	120	Open	0.0088	78.59	
P	*P. guajava*	2.66	68.26	100mL		sunlight	0.0090	76.76	PW
M	*M. oleifera*	2.74	44.57,				0.0047	145.3	
A	*A. indica*	2.92	60.72				0.0074	92.92	
CeO_2 NPs	*Aegle marmelos*	2.90	MB,98	10 ppm,50mL	180	500-W lamp	0.2038	3.40	19
S	*S. cumuni*	2.66	MB ,93.6			Open	0.0252	30.08	
P	*P. guajava*	2.74	92.80	10 ppm,	120	sunlight	0.0204	33.96	PW
M	*M. oleifera*	2.92	93.28	100mL		(OSL)	0.0024	30.86	
A	*A. indica*		93.71				0.0231	29.98	
ZnO_W,23.6 nm	Water		CR ,70.04	50 ppm, 100mL	60	Solar light	0.0132	52.51	22
Hexagonal									
ZnO-SG, 50 nm		3.26	Phenol,85			Solar Light	0.0155	44.72	23
HxR	chemical			50 ppm	120	photo radiometer			
ZnO-PP,100nm		3.28	100			(PMA2200 at 90	0.0312	22.21	
HxW						W/m^2)			
PVA/ZnO, ~70	PVA	3.09	CV, 48	1mg/100mL	90	sunlight	0.00694	100.4	24
S	*S. cumuni*	2.90	CR ,50.52				0.0056	138.8	
P	*P. guajava*	2.66	42.58	10 ppm,		OSL	0.0046	150.3	PW
M	*M. oleifera*	2.74	37.33	100mL	120		0.0039	174.2	
A	*A. indica*	2.92	56.07				0.0071	97.6	
ZnO,250-500 nm	NH_4OH	-	MB, 95.34	100ppm,	150	UV-light.	0.064	10.83	26
Nest like	Hydrothermal			100 mL					
Zn/Ag (1%)	chitosan	3.22	MB, 79.1	6.4 ppm,	240	Hg, lamp	0.0067	103.5	29
				100mL					
ZnO, spherical	egg white	3.28	MB, 100	10ppm, 50mL	55	8 W, UV lamps	0.158	0.158	30
ZnO ,56 ,Hx W	*Hylocereus polyrhizus*	3.36	MB, 95	20ppm, 50mL	120	Sunlight	0.0145	47.80	31
ZnO, 40-60 nm	*Clerodendrum*	3.1	MB, 86	6.39 ppm, 20	60	500 W Xe lamp	ND	-	33
spherical	*phlomidis*								
ZnO-J1, 20-40	*Hibiscus sabdariffa*	2.96	MB, 97	15 ppm,	150	500 W,UV lamp	0.0182	38.08	34
ZnO,32.8 nm			CV, 76	15ppm,30 mL	90		0.011	63.01	
HxW	*Garcinia Cambogia*	3.24	PR, 83		120	25W, UV lamp	0.0067	103.4	35
ZnO, 42.23, Hx	*Myristica fragrans*	3.29	MB, 88	20 ppm, 45	140	UV light	ND		36
ZnO,21, spherical;	*Garcinia mangostana*	3.32	MG, 99	10ppm ,50 mL	180	Solar light	0.0245	28.29	38
ZnO,19, spherical	*Zizyphus jujuba*	3.36	ECBT, 86	100ppm,15mL	300	Sunlight	0.0067	103.4	39
Al-ZnO, 50 nm	*Amomum longiligulare*	ND	MG, 38.1	50μM,	60	UV light	0.008	86.65	40
tetrameric			MB, 66			(CL-1000)	0.014	49.51	
ZnO, nano Flower	*C.haematocephala*	ND	MB, 88,	20ppm,100mL	270	Solar light	0.01	69.32	43
ZnO,14 nm	*Brassica oleracea L*	4.09	PR, 71	$5x10^{-2}$ M	180	250 W He	0.0066	105.0	45
spherical			MB, 74	25 mL		(Helium) lamp	0.0073	94.95	
ZnO,15.6	*Phoenix roebelenii*	3.24	MB,98	10 ppm	105	250W ,UV lamp	0.037	18.8	47
spherical									
ZnO, 10-20 nm	*Morinda umbellata*	2.75	MG, 98.9	20,10ppm,0.1L,	90	UV light	0.0204	33.98	48
spherical			CR,92.8	at pH 10&6			0.0123	56.35	
ZnO,20.17nm	*H. hamnoides*	ND	MG,89	10 ppm	180	UV	ND	-	50
Flower like			EY,95						
S	*S. cumuni*	2.90	EY, 43.72	10 ppm		OSL	0.00472	146.8	
P	*P. guajava*	2.66	38.52	100 mL	120		0.00382	181.5	PW
M	*M. oleifera*	2.74	52.19				0.00551	125.8	
A	*A. indica*	2.92	66.47				0.00506	136.9	
ZnO,20 nm	*Alchemilla vulgaris*	3.27	RhB,75	10 ppm,80 mL	120	500 W Xe lamp	ND	-	51
cauliflower						SHBC XSS-5XD			
ZnO pure	*Synadium grantii*	3.10	IC,26.5	10 ppm,		30 W	0.0192	36.10	
ZnO-Cu(3%)		3.20	IC,78.2	100 mL	80	UV (254nm)	0.0301	23.02	52
ZnO,19.31	*Epipremnum aureum*	3.73	CR,56.6	10 ppm	100	UV	0.014	49.51	53
ZnO ,26.14	*Salvia officinalis*	2.96	MO, 92.47	5 ppm,100mL	120	500W Hg lamp	0.02134	32.48	54
ZnO ,11.35 nm	*S. Cumini*	3.32	MB,91.4	40ppm,50 mL	180	UV–vis	0.004	173.3	55
ZnF-CA-LP	*P. guajava*	-	MB, 96	5 ppm,50mL	120	UV lamp	0.0165	42.01	57
ZnO ,40.05 nm	*M. oleifera*	3.02	MB,80	3.2ppm,50 mL	60	300 W, Halogen	0.013	53.32	60
ZnO-G,18 nm	*Annona Muricata*	3.25	BCB,95	100ppm,100mL	210	254 nm UV lamp	0.0144	48.13	69
S	*S. cumuni*	2.90	52.27	10ppm ,100mL	120	OSLI	0.00651	106.4	
A	*A. indica*	2.92	58.28				0.00708	97.9	PW

gCN/ZnO (50%) M A	ZAD and Urea *M. oleifera* *S. cumuni*	2.03 2.74 2.92	Rb171,89.2 Rb171,70.4 54.16	10ppm,100mL	140 120	Sunlight OSL	0.0150 0.00807 0.00567	46.21 85.89 122.3	71 PW
ZnO,9-18	*corriandrum sativum*	ND	$C_{14}H_{10}$, 96	0.1ppm	240	2 UV lamps,20W	0.009	77.02	72
Ag/ZnO sf	*Hydrothermal*	3.09	MO,99.7 RhB,99.3	10ppm,80mL at 8.8 and 8.7 pH	35	UV, Xenon lamp	0.1104 0.0542	6.27 12.78	73
ZnO ($C_{3\%}$),47 nm	**Laser method**	3.30	RhB, ≈13.8	9.58ppm,	20	Hg UV	0.0074	93.5	74
ZnO, 20-25 nm HxW	Chemical	ND	MO,99.7 CR,97.5 DB38,89.5	30ppm 50 mL	30	1000-W UV lamp	0.1578 0.1119 0.0803	4.39 6.19 8.63	75
ZnO (disklike)	Sol gel, NH_4OH		RhB,85.14	~4.8 ppm,20mL	80	360 W, UV	0.0431	16.08	76

[a] CR F_3BS= coraleneredF3BS, RY =Reactive yellow, Hxw= Hexagonal wurtzite, AR27= Acid red 27, DB38=Direct blue, CV= crystal violet, Acid Blue 92, AB92, TY= Titan Yellow, AMP= acetaminophen, SDZ =sulfadiazine

OSL= open sunlight, RBB= Remazol Brilliant Blue, MOR=Mordenite

In above sequence, extract of seed of *Nephelium lappaceum* [42], leaf of *Pedalium murex* [44], *Calotropis procera* [46], *Calotropis procera* [49], were used to syntheised flower, nanostructure (NS), spherical and rod shaped ZnO photocatalyst which achieved up to 97% (0.05ppm,25ml MB), 91.36%(100mL, MB), 81%(MO) and 92%(100 mL of 10 ppm ,MG) dye removal efficiency (RE) in UV radiation. In a related study, Iron oxide NPs(BGE,2.1 eV), synthesized by Adhikari et al. [56] from *P.guajava* leaf extract achieved ~82.1% and 53.9 % degradation of MB and MO (25 ppm, 250mL) after 95 and 205 min under sunlight irradiation, respectively [56]. ZnO with particle size 52nm and HxW morphology prepared from *M. Oleifera* leaf extract achieved 96 % degradation of 100 ml of TY(83 ppm) after 60 min under sunlight. [58]. Haque *et al.* [61] achieved 80.2% PD of MB using ZnO BNps (BGE,3.2eV) after 200 min, whereas Sanjeev *et al.* [63] noticed 69 %, AMP($C_8H_9NO_2$) and 64 % SDZ($C_{10}H_{10}N_4O_2S$), degradation under 15 min UV light, applying ZnO Nps derived from *A. indica* leaves extract and $Zn(NO_3)2.6H_2O$. Mohaghegh *et al.* [77] developed 25% ZnO/MOR nanocomposite via hydrothermal precipitation techniques, and monitored 88% PD of AB92 (20ppm) in 120 min UV lamp exposure. Similarly, Zouhier *et al.*[78] prepared visible light active ternary composites ZnO/$ZnFe_2O_4$ with reduced BGE, 2.36 eV, by combustion method exhibited 84% and 91% mineralization of 20mg/L RBB ($C_{22}H_{16}N_2Na_2O_{11}S_3$) and MB in 60 min of 25 W UV light source. EL-Dafrawy *et.al* [79] synthesized narrow band gap (3.55 eV), ZnO/7PVA via chemical routes, and successfully applied it more than 15 % UV-driven MB dye degradation.

Ngoepe *et al.* [80] reported the synthesis of ZnO HxW having size of 5-15 nm utilizing *Monsonia burkeana* leaf extract and evaluated 48% RE over 250mL of 20ppm MB dye in 40 min under 40W UV LED. Moreover, Siripireddy *et al.* [81] demonstrated that the addition of 30 mg phyto derived ZnO NPs from *Eucalyptus globulus* leaves extract resultant 98.3% PCD of MO dye. Plants and their part extract namely *Scutellaria baicalensis* [82],*Amomum longiligulare* [83], *Laurus nobilis* [84], *S. Cumini* [85], *Lycopersicon esculentum* [86] have been reported for botanically reduced ZnO NPs for 98.6%, 38.1%, 99%, 98% and 97% degradation of MB,MG,RBRF3B,RhB and MB dyes under light illumination .

3.5 Reusability and Stability of ZnO NS sample

The durability and reusability of the synthesised ZnO NS were assessed through three consecutive experiments run over MB and CR degradation under visible light of 120 min. After each run, the photocatalyst was separated by centrifugation, washed and, dry and followed by filtering and drying in an oven at 100°C for 1 hr. As shown in Fig.14 (a-b), the photocatalytic efficiency reduced to (84 % for MB) and (40 % for CR) by the third cycle. This decline and deactivation in the efficiency of the photocatalyst is observed due to the loss of catalyst through leaching, adsorbed impurities, and

the obstruction of pores by dye molecules. XRD and FTIR, analysis has been shown in Fig.S2 (a-b) confirms that the phase composition and crystallinity of the recycled ZnO NS samples slightly change throughout the process, which corroborates its chemical stability.

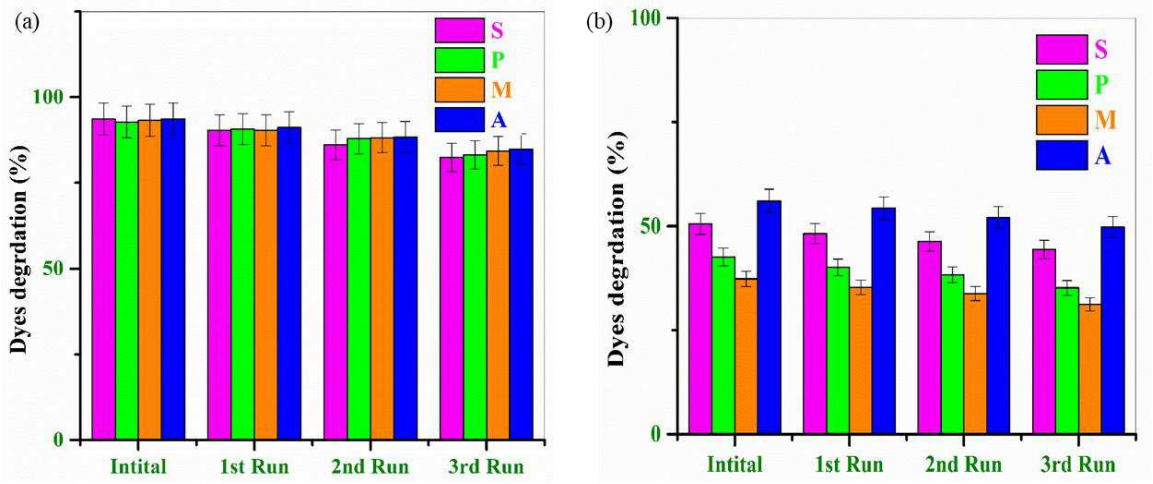


Fig.14. Reusability photodegradation testing of ZnO NS for degradation (a) MB, (b) CR, (0.1 g photocatalyst in 100 ml of 10 ppm dye solution)

3.6 Plausible mechanism of dye degradation

The band edge potential along with the feasibility of reactive oxygen species (ROS) generation of the synthesized ZnO sample containing different phytoconstituents proportions was estimated using the electronegativity method [18] and tabulated in Table.6

Table.6 Band gap energy (*Eg*), estimated conduction band (CB) and valence band (VB) edge potentials of ZnO NS and

ZnO NS Sample	Band gap (eV)	Band gap position vs Normal Hydrogen Electrode (NHE)*			
		CB (eV)	CB Function	VB (eV)	VB Function
		$E_{CB}=X-Ee-2Eg$	$O_2 \rightarrow \bullet O_2^-$(-0.33 eV) $\cdot O_2^- \rightarrow H_2O_2$	$E_{VB}=E_{CB}+Eg$	$OH^- \rightarrow \bullet OH$ (+2.38
S	2.90	-0.16	Non feasible	+2.74	Strongly possible
P	2.66	-0.04		+2.62	
M	2.74	-0.08		+2.66	
A	2.92	-0.17		+2.75	

*X= Absolute electronegativity of ZnO (5.79 eV), and Ee is the energy of free electrons on the hydrogen scale (4.5 eV)

The photocatalytic reaction (PCR) starts, when sun light bearing energy that corresponds to or exceeds the ZnO band gap (2.66-2.92 eV) triggers the excitation of electrons from VB to CB. This migration creates essential e-/h+ pairs, via surface plasmon resonance, Eq. (7) as shown in Fig.15[29].

$$ZnO\ NS + h\upsilon_{(SL)} \rightarrow e^-_{(CB)} + h^+_{(VB)}\ pair \quad (7)$$

Since VB position of ZnO NS (+2.62 to 2.75 eV vs NHE) was sufficiently positive to generate dominant reactive hydroxyl radicals ($OH^{\cdot}$) through interaction of holes (h+) with H_2O and OH^- ions. [27-29]. Since CB position for all sample were found to be much less negative (-0.04 to -0.16 eV) than $O_2/\bullet O_2^-$ redox potential (-0.33eV) hence, the formation of secondary superoxide radicals ($O_2/^{\bullet}O_2^-$) and generation of H_2O_2 via superoxide-mediated pathways ($\bullet O_2^- \rightarrow H_2O_2$) is

thermodynamically unfavorable. Hence •OH radical and photogenerated holes (h^+) primarily target the systematic splits of specific bond (C-C,C=C,C=O,C-N, C=N) of dye molecule, into smaller aromatic intermediates before achieving the mineralization of the dye to produce colourless, and nontoxic products, after a series of reaction (8) to (12)[18,31,35,37-39].

$$H_2O \rightarrow H^+ + OH^- \quad (8)$$

$$ZnO\ NS\ \{h^+_{(VB)}\} + H_2O + OH^- \rightarrow \bullet OH \quad (9)$$

$$MB + h^+ \rightarrow C_6H_5OH + CH_2{=}CH\text{-}CH{=}N\text{-}OH\ (m/z{=}71.44) \quad (10)$$

$$MG + \bullet OH \rightarrow\rightarrow \text{intermediate} \rightarrow\rightarrow CH_3COOH\ (m/z{=}61) \quad (11)$$

$$BCB/Rb171/CR/EY\ dye + \bullet OH + h^+ \rightarrow \text{Degraded Products} \quad (12)$$

The efficacy degradation is further improved by electrostatic attraction. As MB, MG and BCB dissolve in dH_2O, they turn positively charged and thus easily adsorb onto the negatively charged surface of the ZnO NS. Interestingly, a study by Aniruddha *et al.* [87] indicates that the degradation may not be merely light dependent, but reductive characteristics of ZnO NS may be playing important role in generation of e^-/h^+ pairs even in the dark. This spontaneous generation of ROS on the surface of the S, P, M and A offers an alternative mechanism for degradation of MG, BCB and CR dyes, within higher times, proving the versatile applicability of such catalysts to the environment.

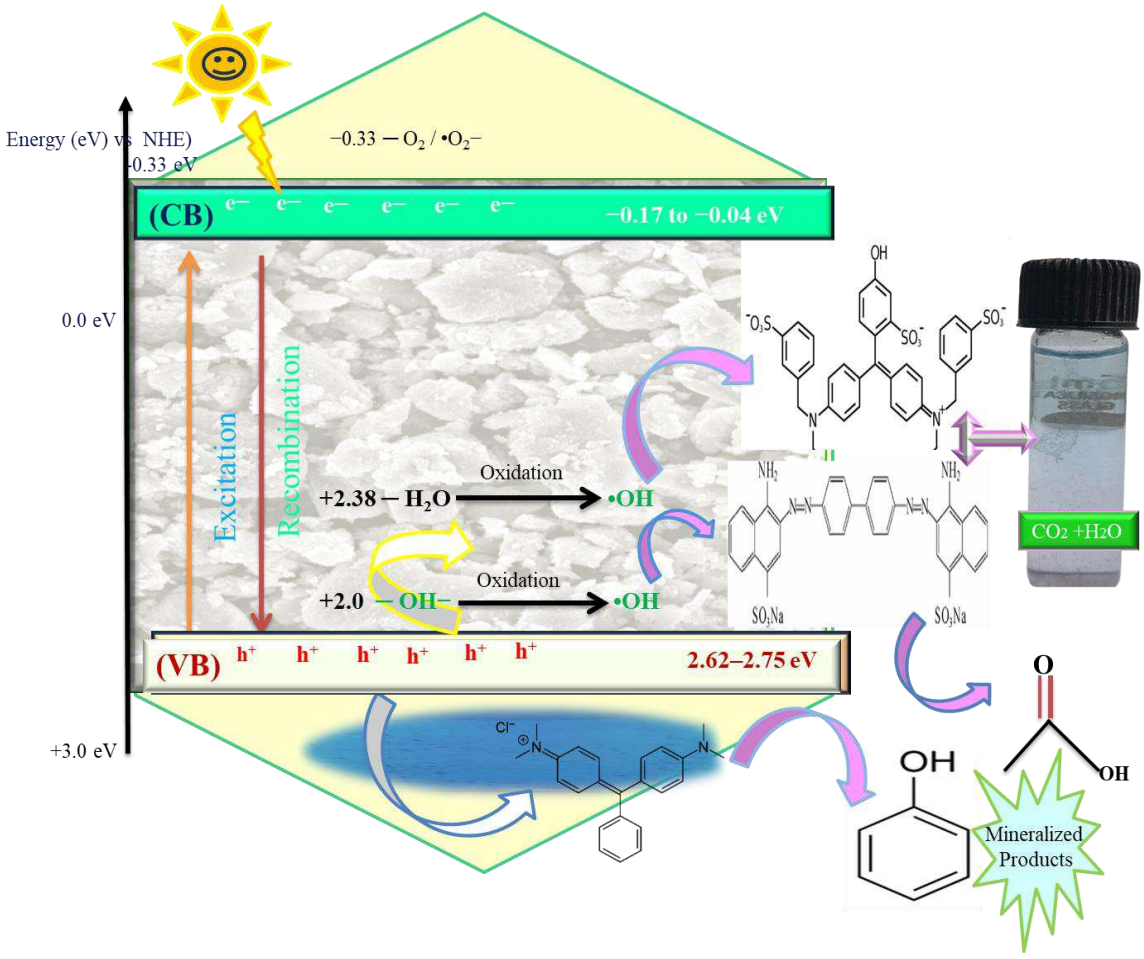


Fig.15 Plausible mechanism for photodegradation of examined cationic and anionic in open solar light irradiation

4.Conclusion

This study introduced a phytofabricated method for the synthesis of ZnO NS samples, namely S, P, M and A, utilising leaf extract of *S. cumini, P. guajava, M. oleifera and A. indica* and $(CH_3COO)Zn.2H_2O$ as a source of precursor ions. FTIR, FESEM and XRD revealed plant-based polyphenols, carboxylic acids and alkaloids drive the biochemical synthesis of irregular, flake-like hexagonal wurtzite ZnO NS with a mean crystalline size range of 6.66-16.93 nm and band gap energy 2.66-2.92 eV, while EDX verified almost homogeneous Zn-O distribution. Calculated zeta potential ZnO NS for samples S, P, M and A were found to be -23.7 to -28.6 mV, confirming their colloidal stability for adsorption of cationic dye on their surface. ZnO NS samples P and A demonstrated excellent photocatalytic performance, achieving 92.80% and 93.71% degradation of MB under OSLI within 120 min, whereas sample M exhibited 70.37% photodegradation efficiency for Rb171 dye. Similarly, sample A demonstrated degradation rates of 56.07% for CR and 66.47% for Ey dye. This efficiency stems from structural attributes particularly the smaller size, dislocation density, microstrain, surface defects and reduced electron-hole recombination of the green synthesised ZnO NS sample and highlights a sustainable solution for effective degradation of organic dyes from textile wastewater.

Credit author statements

Suneel: Methodology, synthesis, analysis, testing, writing original draft, validation and language correction, **Haroon**: Visualization, validation, and correction of the original draft **M.S;** Technical support, **Z.F**.; Technical support, help in analysis of sample. **N. Ahamad;** Introduction, language correction, **Q.I.R.;** Supervision, Visualization, Conceptualization, and corrections to original draft. All authors have read and agreed to the published version of manuscript.

Funding: This research receives no external funding.

Institutional Review Board Statement: Not applicable

Informed Consent Statement: Not applicable.

Data Availability Statement:

All relevant data are included in the paper or its Supplementary Information.

Declaration of Conflicts of Interest: The authors report no conflict of interest.

Acknowledgments: The authors extend their appreciation to the department of Botany, University of Lucknow, for identification and taxonomy of plants leaves. The authors gratefully to Integral Centre of Excellence for interdisciplinary Research (ICEIR) for providing facilities and technical support & Development section to provide the manuscript communication number (**IU/R&D/2024-MCN0003110)** and last but not least to MIT, Jaipur for characterization of the sample.

References:

[1] Adesanmi BM, Hung YT, Paul H, Huhnke C. Comparison of dye wastewater treatment methods: A review. GSC Advanced Research and Reviews, 10 (2). 2022;10(2):126. https://doi.org/10.5281/zenodo.6331586

[2] Liu Q. Pollution and treatment of dye waste-water. InIOP conference series: earth and environmental science 2020 May 1 (Vol. 514, No. 5, p. 052001). iop publishing. https://**doi:10.1088/1755-1315/514/5/052001**

[3] Bafana A, Devi SS, Chakrabarti T. Azo dyes: past, present and the future. Environmental Reviews. 2011 Dec;19(NA):350-71. https://doi.org/10.1139/a11-018

[4] Dyes & Pigments Market Size, Share, Trends & Forecast https://www.omrglobal.com

[5] Lellis B, Fávaro-Polonio CZ, Pamphile JA, Polonio JC. Effects of textile dyes on health and the environment and bioremediation potential of living organisms. Biotechnology research and innovation. 2019 Jul 1;3(2):275-90. https://doi.org/10.1016/j.biori.2019.09.001

[6] Al-Tohamy R, Ali SS, Li F, Okasha KM, Mahmoud YA, Elsamahy T, Jiao H, Fu Y, Sun J. A critical review on the treatment of dye-containing wastewater: Ecotoxicological and health concerns of textile dyes and possible remediation approaches for environmental safety. Ecotoxicology and environmental safety. 2022 Feb 1;231:113160.
https://doi.org/10.1016/j.ecoenv.2021.113160

[7] Benkhaya S, M'rabet S, El Harfi A. Classifications, properties, recent synthesis and applications of azo dyes. Heliyon. 2020 Jan 1;6(1). https://doi.org/10.1016/j.heliyon.2020.e03271

[8] Dutta S, Gupta B, Srivastava SK, Gupta AK. Recent advances on the removal of dyes from wastewater using various adsorbents: A critical review. Materials Advances. 2021;2(14):4497-531. DOI: 10.1039/D1MA00354B

[9] Holkar CR, Jadhav AJ, Pinjari DV, Mahamuni NM, Pandit AB. A critical review on textile wastewater treatments: possible approaches. Journal of environmental management. 2016 Nov 1;182:351-66. http://dx.doi.org/10.1016/j.jenvman.2016.07.090

[10] Selvaraj V, Karthika TS, Mansiya C, Alagar MJ. An over review on recently developed techniques, mechanisms and intermediate involved in the advanced azo dye degradation for industrial applications. Journal of molecular structure. 2021 Jan 15;1224:129195. https://doi.org/10.1016/j.molstruc.2020.129195

[11] Katheresan V, Kansedo J, Lau SY. Efficiency of various recent wastewater dye removal methods: A review. Journal of environmental chemical engineering. 2018 Aug 1;6(4):4676-97. https://doi.org/10.1016/j.jece.2018.06.060

[12] Lim NY, Chiam SL, Leo CP, Chang CK. Recent modification, mechanisms, and performance of zinc oxide-based photocatalysts for sustainable dye degradation. Hybrid Advances. 2024 Dec 1;7:100318. https://doi.org/10.1016/j.hybadv.2024.100318

[13] Ren G, Han H, Wang Y, Liu S, Zhao J, Meng X, Li Z. Recent advances of photocatalytic application in water treatment: A review. Nanomaterials. 2021 Jul 12;11(7):1804. https://doi.org/10.3390/nano11071804

[14] Bopape DA, Ntsendwana B, Mabasa FD. Photocatalysis as a pre-discharge treatment to improve the effect of textile dyes on human health: A critical review. Heliyon. 2024 Oct 30;10(20). https://doi.org/10.1016/j.heliyon.2024.e39316

[15] Kumari H, Sonia, Suman, Ranga R, Chahal S, Devi S, Sharma S, Kumar S, Kumar P, Kumar S, Kumar A. A review on photocatalysis used for wastewater treatment: dye degradation. Water, Air, & Soil Pollution. 2023 Jun;234(6):349. https://doi.org/10.1007/s11270-023-06359-9

[16] Ajibade PA, Oluwalana AE. Enhanced photocatalytic degradation of ternary dyes by copper sulfide nanoparticles. Nanomaterials. 2021 Aug 4;11(8):2000.https://doi.org/10.3390/nano11082000

[17] Shahadat A, Ahmed W, Haroon U, Ahmed K. Azadirachta indica (Neem) fruit latex-based iron oxide magnetic nanoparticles (FeO-MNPs): Synthesis and green treatment of reactive yellow RY-176 dye. GLOBAL NEST JOURNAL. 2025 Jan 1;27(9). https://doi.org/10.30955/gnj.07274

[18] Veg E, Raza A, Rai S, Bansal P, Sharma S, Mishra N, Gupta R, Mishra S, Joshi S, Khan AR, Khan T. Green synthesis of ZnO and α-Fe 2 O 3 nanoparticles using Chinese fan palm leaf extract for their biological and photocatalytic activity evaluation. RSC Sustainability. 2025;3(12):5609-31. DOI: 10.1039/D5SU00349K

[19] Jayakodi S, Sriramulu M, Govindasamy M, Pandian E, Shanmugam R, Ameen F. Visible light photocatalytic degradation and biological activities of Aegle marmelos-mediated cerium oxide nanoparticles. Green Process. Synth. 13 (1), 20240060 (2025) [Internet]. 2024 https://doi.org/10.1515/gps-2024-0060

[20] Gnanaprakasam A, Sivakumar VM, Sivayogavalli PL, Thirumarimurugan M. Characterization of TiO2 and ZnO nanoparticles and their applications in photocatalytic degradation of azodyes. Ecotoxicology and environmental safety. 2015 Nov 1;121:121-5. http://dx.doi.org/10.1016/j.ecoenv.2015.04.043

[21] Rezapour M, Talebian N. Comparison of structural, optical properties and photocatalytic activity of ZnO with different morphologies: Effect of synthesis methods and reaction media. Materials Chemistry and Physics. 2011 Sep 15;129(1-2):249-55. https://doi.org/10.1016/j.matchemphys.2011.04.012

[22] Ong CB, Mohammad AW, Rohani R, Ba-Abbad MM, Hairom NH. Solar photocatalytic degradation of hazardous Congo red using low-temperature synthesis of zinc oxide nanoparticles. Process Safety and Environmental Protection. 2016 Nov 1;104:549-57. https://doi.org/10.1016/j.psep.2016.04.006

[23] Uribe-López MC, Hidalgo-López MC, López-González R, Frías-Márquez DM, Núñez-Nogueira G, Hernández-Castillo D, Alvarez-Lemus MA. Photocatalytic activity of ZnO nanoparticles and the role of the synthesis method on their physical and chemical properties. Journal of Photochemistry and photobiology A: Chemistry. 2021 Jan 1;404:112866. https://doi.org/10.1016/j.jphotochem.2020.112866

[24] Premkumar H. Synthesis, characterization and photocatalytic performance of polyvinyl alcohol/zinc oxide nanocomposites: A comprehensive study. Nano-Structures & Nano-Objects. 2024 Sep 1;39:101208. https://doi.org/10.1016/j.nanoso.2024.101208

[25] Hairom NH, Mohammad AW, Kadhum AA. Effect of various zinc oxide nanoparticles in membrane photocatalytic reactor for Congo red dye treatment. Separation and Purification Technology. 2014 Nov 24;137:74-81. http://dx.doi.org/10.1016/j.seppur.2014.09.027

[26] Chaudhari SP, Bodade AB, Chaudhari GN. Synthesis, characterization and photocatalytic recital of nest-like zinc oxide photocatalyst. Korean Journal of Chemical Engineering. 2013 Nov;30(11):2001-6. https://doi.org/10.1007/s11814-013-0151-3

[27] Adam RE, Pozina G, Willander M, Nur O. Synthesis of ZnO nanoparticles by co-precipitation method for solar driven photodegradation of Congo red dye at different pH. Photonics and Nanostructures-Fundamentals and Applications. 2018 Dec 1;32:11-8. https://doi.org/10.1016/j.photonics.2018.08.005

[28] Raula M, Rashid MH, Paira TK, Dinda E, Mandal TK. Ascorbate-assisted growth of hierarchical ZnO nanostructures: sphere, spindle, and flower and their catalytic properties. Langmuir. 2010 Jun 1;26(11):8769-82. https://doi.org/10.1021/la904507q

[29] Messih MA, Ahmed MA, Soltan A, Anis SS. Synthesis and characterization of novel Ag/ZnO nanoparticles for photocatalytic degradation of methylene blue under UV and solar irradiation. Journal of Physics and Chemistry of Solids. 2019 Dec 1;135:109086. https://doi.org/10.1016/j.jpcs.2019.109086

[30] Pudukudy M, Yaakob Z. Facile synthesis of quasi spherical ZnO nanoparticles with excellent photocatalytic activity. Journal of Cluster Science. 2015 Jul;26(4):1187-201. DOI 10.1007/s10876-014-0806-1 https://doi.org/10.1007/s10876-014-0806-1

[31] Aminuzzaman M, Ng PS, Goh WS, Ogawa S, Watanabe A. Value-adding to dragon fruit (Hylocereus polyrhizus) peel biowaste: green synthesis of ZnO nanoparticles and their characterization. Inorganic and Nano-Metal Chemistry. 2019 Nov 2;49(11):401-11. https://doi.org/10.1080/24701556.2019.1661464

[32] Fouda A, Saied E, Eid AM, Kouadri F, Alemam AM, Hamza MF, Alharbi M, Elkelish A, Hassan SE. Green synthesis of zinc oxide nanoparticles using an aqueous extract of Punica granatum for antimicrobial and catalytic activity. Journal of Functional Biomaterials. 2023 Apr 7;14(4):205.
https://doi.org/10.3390/jfb14040205

[33] Ravichandran S, Radhakrishnan J, Sengodan P, Rajendran R, Ramalingam R, Arunachalam KD. Bio synthesis of Zinc oxide nanoparticles using Clerodendrum phlomidis extract for antibacterial, anticancer, antioxidant and photocatalytic studies. Journal of Materials Science: Materials in Electronics. 2022 May;33(14):11455-66. https://doi.org/10.1007/s10854-022-08118-8

[34] Soto-Robles CA, Luque PA, Gómez-Gutiérrez CM, Nava O, Vilchis-Nestor AR, Lugo-Medina E, Ranjithkumar R, Castro-Beltrán A. Study on the effect of the concentration of Hibiscus sabdariffa extract on the green synthesis of ZnO nanoparticles. Results in Physics. 2019 Dec 1;15:102807. https://doi.org/10.1016/j.rinp.2019.102807

[35] Sasi S, Fasna PF, Sharmila TB, Chandra CJ, Antony JV, Raman V, Nair AB, Ramanathan HN. Green synthesis of ZnO nanoparticles with enhanced photocatalytic and antibacterial activity. Journal of Alloys and Compounds. 2022 Nov 30;924:166431 https://doi.org/10.1016/j.jallcom.2022.166431.

[36] Faisal S, Jan H, Shah SA, Shah S, Khan A, Akbar MT, Rizwan M, Jan F, Wajidullah, Akhtar N, Khattak A. Green synthesis of zinc oxide (ZnO) nanoparticles using aqueous fruit extracts of Myristica fragrans: their characterizations and biological and environmental applications. ACS omega. 2021 Mar 30;6(14):9709-22. http://pubs.acs.org/journal/acsodf

[37] Rupa EJ, Anandapadmanaban G, Mathiyalagan R, Yang DC. Synthesis of zinc oxide nanoparticles from immature fruits of *Rubus coreanus* and its catalytic activity for degradation of industrial dye. Optik. 2018 Nov 1;172:1179-86. https://doi.org/10.1016/j.ijleo.2018.07.115

[38] Aminuzzaman M, Ying LP, Goh WS, Watanabe A. Green synthesis of zinc oxide nanoparticles using aqueous extract of Garcinia mangostana fruit pericarp and their photocatalytic activity. Bulletin of Materials Science. 2018 Apr;41(2):50. https://doi.org/10.1007/s12034-018-1568-4

[39] Golmohammadi M, Honarmand M, Ghanbari S. A green approach to synthesis of ZnO nanoparticles using jujube fruit extract and their application in photocatalytic degradation of organic dyes. Spectrochimica Acta Part A: Molecular and Biomolecular Spectroscopy. 2020 Mar 15;229:117961.
https://doi.org/10.1016/j.saa.2019.117961

[40] Liu YC, Li J, Ahn J, Pu J, Rupa EJ, Huo Y, Yang DC. Biosynthesis of zinc oxide nanoparticles by one-pot green synthesis using fruit extract of Amomum longiligulare and its activity as a photocatalyst. Optik. 2020 Sep 1;218:165245 https://doi.org/10.1016/j.ijleo.2020.165245.

[41] Davar F, Majedi A, Mirzaei A. Green synthesis of ZnO nanoparticles and its application in the degradation of some dyes. Journal of the American Ceramic Society. 2015 Jun;98(6):1739-46.
https://doi.org/10.1111/jace.13467

[42] Kuruppu KA, Perera KM, Chamara AM, Thiripuranathar G. Flower shaped ZnO—NPs; phytofabrication, photocatalytic, fluorescence quenching, and photoluminescence activities. Nano. Express 1, 020020 (2020) [Internet]. 2020 https://doi.org/10.1088/2632-959X/aba862

[43] Vinayagam R, Selvaraj R, Arivalagan P, Varadavenkatesan T. Synthesis, characterization and photocatalytic dye degradation capability of Calliandra haematocephala-mediated zinc oxide nanoflowers. Journal of Photochemistry and Photobiology B: Biology. 2020 Jan 1;203:111760. https://doi.org/10.1016/j.jphotobiol.2019.111760

[44] Babitha N, Priya LS, Christy SR, Manikandan A, Dinesh A, Durka M, Arunadevi S. Enhanced antibacterial activity and photo-catalytic properties of ZnO nanoparticles: Pedalium murex plant extract-assisted synthesis. Journal of nanoscience and nanotechnology. 2019 May 1;19(5):2888-94. https://doi:10.1166/jnn.2019.16023

[45] Osuntokun J, Onwudiwe DC, Ebenso EE. Green synthesis of ZnO nanoparticles using aqueous Brassica oleracea L. var. italica and the photocatalytic activity. Green chemistry letters and reviews. 2019 Oct 2;12(4):444-57. https://doi.org/10.1080/17518253.2019.1687761

[46] Gawade VV, Gavade NL, Shinde HM, Babar SB, Kadam AN, Garadkar KM. Green synthesis of ZnO nanoparticles by using Calotropis procera leaves for the photodegradation of methyl orange. Journal of Materials Science: Materials in Electronics. 2017 Sep;28(18):14033-9. https://DOI 10.1007/s10854-017-7254-2

[47] Aldeen TS, Mohamed HE, Maaza M. ZnO nanoparticles prepared via a green synthesis approach: Physical properties, photocatalytic and antibacterial activity. Journal of Physics and Chemistry of Solids. 2022 Jan 1;160:110313. https://doi.org/10.1016/j.jpcs.2021.110313

[48] Sreelekshmi PB, Pillai RR, Unnimaya S, Anju AL, Meera AP. Biofabrication of novel ZnO nanoparticles for efficient photodegradation of industrial dyes. Clean Technologies and Environmental Policy. 2024 Nov;26(11):3805-18. https://doi.org/10.1007/s10098-023-02469-4

[49] Vasantharaj S, Sathiyavimal S, Senthilkumar P, Kalpana VN, Rajalakshmi G, Alsehli M, Elfasakhany A, Pugazhendhi A. Enhanced photocatalytic degradation of water pollutants using bio-green synthesis of zinc oxide nanoparticles (ZnO NPs). Journal of Environmental Chemical Engineering. 2021 Aug 1;9(4):105772. https://doi.org/10.1016/j.jece.2021.105772

[50] Rupa EJ, Anandapadmanaban G, Chokkalingam M, Li JF, Markus J, Soshnikova V, Perez ZE, Yang DC. Cationic and anionic dye degradation activity of Zinc oxide nanoparticles from Hippophae rhamnoides leaves as potential water treatment resource. Optik. 2019 Mar 1;181:1091-8. https://doi.org/10.1016/j.ijleo.2018.12.152

[51] Rajendrachari S, Taslimi P, Karaoglanli AC, Uzun O, Alp E, Jayaprakash GK. Photocatalytic degradation of Rhodamine B (RhB) dye in waste water and enzymatic inhibition study using cauliflower shaped ZnO nanoparticles synthesized by a novel One-pot green synthesis method. Arabian Journal of Chemistry. 2021 Jun 1;14(6):103180. https://doi.org/10.1016/j.arabjc.2021.103180

[52] Karthik KV, Raghu AV, Reddy KR, Ravishankar R, Sangeeta M, Shetti NP, Reddy CV. Green synthesis of Cu-doped ZnO nanoparticles and its application for the photocatalytic degradation of hazardous organic pollutants. Chemosphere. 2022 Jan 1;287:132081. https://doi.org/10.1016/j.chemosphere.2021.132081

[53] Brishti RS, Ahsan Habib M, Ara MH, Rezaul Karim KM, Khairul Islam M, Naime J. Green synthesis of ZnO NPs using aqueous extract of Epipremnum aureum leave: Photocatalytic degradation of Congo red. Results Chem. 2024; 7: 101441 [Internet]. 2024 https://doi.org/10.1016/j.rechem.2024.101441

[54] Abomuti MA, Danish EY, Firoz A, Hasan N, Malik MA. Green synthesis of zinc oxide nanoparticles using salvia officinalis leaf extract and their photocatalytic and antifungal activities. Biology. 2021 Oct 21;10(11):1075. https://doi.org/10.3390/biology10111075

[55] Sadiq H, Sher F, Sehar S, Lima EC, Zhang S, Iqbal HM, Zafar F, Nuhanović M. Green synthesis of ZnO nanoparticles from Syzygium Cumini leaves extract with robust photocatalysis applications. Journal of Molecular Liquids. 2021 Aug 1; 335:116567. https://doi.org/10.1016/j.molliq.2021.116567

[56] Adhikari A, Chhetri K, Acharya D, Pant B, Adhikari A. Green synthesis of iron oxide nanoparticles using Psidium guajava L. leaves extract for degradation of organic dyes and anti-microbial applications. Catalysts. 2022 Oct 7;12(10):1188. https://doi.org/10.3390/catal12101188

[57] Fahim YA, El-Khawaga AM, Sallam RM, Elsayed MA, Assar MF. Immobilized lipase enzyme on green synthesized magnetic nanoparticles using Psidium guava leaves for dye degradation and antimicrobial activities. Scientific Reports. 2024 Apr 17;14(1):8820. https://doi.org/10.1038/s41598-024-58840-y

[58] Pal S, Mondal S, Maity J, Mukherjee R. Synthesis and characterization of ZnO nanoparticles using Moringa oleifera leaf extract: investigation of photocatalytic and antibacterial activity. Int. J. Nanosci. Nanotechnol. 2018 May 1;14(2):111-9.

[59] Abel S, Tesfaye JL, Nagaprasad N, Shanmugam R, Dwarampudi LP, Krishnaraj R. Synthesis and characterization of zinc oxide nanoparticles using moringa leaf extract. Journal of Nanomaterials. 2021;2021(1):4525770. https://doi.org/10.1155/2021/4525770

[60] Adam F, Himawan A, Aswad M, Ilyas S, Heryanto, Anugrah MA, Tahir D. Green synthesis of zinc oxide nanoparticles using Moringa oleifera l. water extract and its photocatalytic evaluation. InJournal of Physics: Conference Series 2021 Jan (Vol. 1763, No. 1, p. 012002). IOP Publishing. https://doi:10.1088/1742-6596/1763/1/012002

[61] Haque MJ, Bellah MM, Hassan MR, Rahman S. Synthesis of ZnO nanoparticles by two different methods & comparison of their structural, antibacterial, photocatalytic and optical properties. Nano Express. 2020 Jun 1;1(1):010007. https://doi.org/10.1088/2632-959X/ab7a43

[62] Rehana D, Mahendiran D, Kumar RS, Rahiman AK. In vitro antioxidant and antidiabetic activities of zinc oxide nanoparticles synthesized using different plant extracts. Bioprocess and biosystems engineering. 2017 Jun;40(6):943-57,https:// DOI.org/10.1007/s00449-017-1758-2.

[63] Sanjeev NO, Valsan AE, Zachariah S, Vasu ST. Synthesis of zinc oxide nanoparticles from Azadirachta indica extract: a sustainable and cost-effective material for wastewater treatment. Journal of Hazardous, Toxic, and Radioactive Waste. 2023 Oct 1;27(4):04023027. https://doi.org/10.1061/JHTRBP.HZENG-12

[64] Ramos IL, Bandiola TM. Phytochemical screening of Syzygium cumini (Myrtaceae) leaf extracts using different solvents of extraction. Der Pharmacia Lettre. 2017;9(2):74-8.

[65] Adamu A. Phytochemical screening of guava leave extract. International Journal of Pure and Applied Science Research. 2021;12(2):89-95.

[66] Vongsak B, Sithisarn P, Mangmool S, Thongpraditchote S, Wongkrajang Y, Gritsanapan W. Maximizing total phenolics, total flavonoids contents and antioxidant activity of Moringa oleifera leaf extract by the appropriate extraction method. Industrial crops and products. 2013 Jan 1;44:566-71.
http://dx.doi.org/10.1016/j.indcrop.2012.09.021

[67] Matinise N, Fuku XG, Kaviyarasu K, Mayedwa N, Maaza MJ. ZnO nanoparticles via Moringa oleifera green synthesis: Physical properties & mechanism of formation. Applied surface science. 2017 Jun 1;406:339-47. http://dx.doi.org/10.1016/j.apsusc.2017.01.219

[68] Dash SP, Dixit S, Sahoo S. Phytochemical and biochemical characterizations from leaf extracts from Azadirachta Indica: an important medicinal plant. Biochem Anal Biochem. 2017;6(323):2161-1009.
http://dx.doi.org/10.4172/2161-1009.1000323

[69] Alim NA, Malai HS, Isahak WN, Tan AL. Photocatalytic Degradation of Brilliant Green Using ZnO Nanoparticles Synthesized via Green and Chemical Methods. Eurasian Journal of Physics and Functional Materials. 2025;9(4). *https://doi.org/10.69912/2616-8537.1255*

[70] Deka K, Nongbet RD, Das K, Saikia P, Kaur S, Talukder A, Thakuria B. Understanding the mechanism underlying the green synthesis of metallic nanoparticles using plant extract (s) with special reference to Silver, Gold, Copper and Zinc oxide nanoparticles. Hybrid Advances. 2025 Jun 1;9:100399.
https://doi.org/10.1016/j.hybadv.2025.100399

[71] Hasan S, Khan MA, Bano D, Iqbal A, Imran A, Rahman QI. Evaluation of physiochemical properties of g-C3N4/ZnO composites with enhanced photocatalytic activity under sunlight irradiation. Materials Science and Engineering: B. 2026 Feb 1;324:119008. https://doi.org/10.1016/j.mseb.2025.119008

[72] Hassan SS, El Azab WI, Ali HR, Mansour MS. Green synthesis and characterization of ZnO nanoparticles for photocatalytic degradation of anthracene. Advances in Natural Sciences: Nanoscience and Nanotechnology. 2015 Dec 1;6(4):045012. https://doi.org/10.1088/2043-6262/6/4/045012

[73] Lim H, Yusuf M, Song S, Park S, Park KH. Efficient photocatalytic degradation of dyes using photo-deposited Ag nanoparticles on ZnO structures: simple morphological control of ZnO. RSC advances. 2021;11(15):8709-17. https://doi.org/10.1039/D0RA10945B

[74] Blažeka D, Car J, Klobučar N, Jurov A, Zavašnik J, Jagodar A, Kovačević E, Krstulović N. Photodegradation of methylene blue and rhodamine B using laser-synthesized ZnO nanoparticles. Materials. 2020 Sep 30;13(19):4357. https://doi.org/10.3390/ma13194357

[75] Chen X, Wu Z, Liu D, Gao Z. Preparation of ZnO photocatalyst for the efficient and rapid photocatalytic degradation of azo dyes. Nanoscale research letters. 2017 Dec;12(1):143.
https://doi.org/10.1186/s11671-017-1904-4

[76] Pung SY, Lee WP, Aziz A. Kinetic study of organic dye degradation using ZnO particles with different morphologies as a photocatalyst. International Journal of Inorganic Chemistry. 2012;2012(1):608183. https://doi.org/10.1155/2012/608183

[77] Mohaghegh N, Tasviri M, Rahimi E, Gholami MR. Nano sized ZnO composites: Preparation, characterization and application as photocatalysts for degradation of AB92 azo dye. Materials science in semiconductor processing. 2014 May 1;21:167-79. http://dx.doi.org/10.1016/j.mssp.2013.12.023

[78] Zouhier M, Tanji K, Navío JA, Hidalgo MC, Jaramillo-Páez C, Kherbeche A. Preparation of ZnFe2O4/ZnO composite: effect of operational parameters for photocatalytic degradation of dyes under UV and visible illumination. Journal of Photochemistry and Photobiology A: Chemistry. 2020 Mar 1;390:112305. https://doi.org/10.1016/j.jphotochem.2019.112305

[79] El-Dafrawy SM, Tarek M, Samra S, Hassan SM. Synthesis, photocatalytic and antidiabetic properties of ZnO/PVA nanoparticles. Scientific Reports. 2021 Jun 1;11(1):11404. https://doi.org/10.1038/s41598-021-90846-8

[80] Ngoepe NM, Mbita Z, Mathipa M, Mketo N, Ntsendwana B, Hintsho-Mbita NC. Biogenic synthesis of ZnO nanoparticles using Monsonia burkeana for use in photocatalytic, antibacterial and anticancer applications. Ceramics International. 2018 Oct 1;44(14):16999-7006. To
https://doi.org/10.1016/j.ceramint.2018.06.142

[81] Siripireddy B, Mandal BK. Facile green synthesis of zinc oxide nanoparticles by Eucalyptus globulus and their photocatalytic and antioxidant activity. Advanced Powder Technology. 2017 Mar 1;28(3):785-97.
https://doi.org/10.1016/j.apt.2016.11.026

[82] Chen L, Batjikh I, Hurh J, Han Y, Huo Y, Ali H, Li JF, Rupa EJ, Ahn JC, Mathiyalagan R, Yang DC. Green synthesis of zinc oxide nanoparticles from root extract of Scutellaria baicalensis and its photocatalytic degradation activity using methylene blue. Optik. 2019 May 1;184:324-9. https://doi.org/10.1016/j.ijleo.2019.03.051

[83] Liu YC, Li J, Ahn J, Pu J, Rupa EJ, Huo Y, Yang DC. Biosynthesis of zinc oxide nanoparticles by one-pot green synthesis using fruit extract of Amomum longiligulare and its activity as a photocatalyst. Optik. 2020 Sep 1;218:165245. https://doi.org/10.1016/j.ijleo.2020.165245

[84] Chemingui H, Missaoui T, Mzali JC, Yildiz TU, Konyar M, Smiri M, Saidi N, Hafiane A, Yatmaz HC. Facile green synthesis of zinc oxide nanoparticles (ZnO NPs): Antibacterial and photocatalytic activities. Materials Research Express. 2019 Oct 1;6(10):1050b4. **https://doi.org/**10.1088/2053-1591/ab3cd6

[85] Rafique M, Tahir R, Gillani SS, Tahir MB, Shakil M, Iqbal T, Abdellahi MO. Plant-mediated green synthesis of zinc oxide nanoparticles from Syzygium Cumini for seed germination and wastewater purification. International Journal of Environmental Analytical Chemistry. 2022 Jan 2;102(1):23-38. https://doi.org/10.1080/03067319.2020.1715379

[86] Nava OJ, Soto-Robles CA, Gómez-Gutiérrez CM, Vilchis-Nestor AR, Castro-Beltrán A, Olivas A, Luque PA. Fruit peel extract mediated green synthesis of zinc oxide nanoparticles. Journal of Molecular Structure. 2017 Nov 5;1147:1-6. https://doi.org/10.1016/j.molstruc.2017.06.078

[87] Molla A, Sahu M, Hussain S. Under dark and visible light: fast degradation of methylene blue in the presence of Ag–In–Ni–S nanocomposites. Journal of Materials Chemistry A. 2015;3(30):15616-25. DOI: 10.1039/C5TA02888D

Supplementary Files

This is a list of supplementary files associated with this preprint. Click to download.

- SupplymentoryFile.docx